Folate receptor beta as an imaging target in myocardial infarction

T M Arman Hossain Anand

Master's Thesis

Master's Degree Programme in Biomedical Imaging

Supervisors:

Prof. Anne Roivainen

Professor, Preclinical Imaging and Drug Research

Turku PET Centre

Prof. Antti Saraste

Professor, Internal Medicine

Heart Center, Turku University Hospital

Research field: In vivo & clinical imaging

Faculty of Medicine, Institute of Biomedicine, University of Turku, Turku PET Centre

Åbo Akademi University
Master's Degree Programme in Biomedical Imaging
Faculty of Science and Engineering

T M Arman Hossain Anand

Title of the thesis:
Folate receptor beta as an imaging target in myocardial infarction

Master's Thesis
PET Imaging
April 2023

Abstract

For decades, myocardial infarction (MI) has been one of the leading causes of mortality worldwide. MI is characterized by different stages of inflammation of myocardium up to subsequent fibrosis. During the inflammatory process, macrophage population increases and the expression of FR-β on their surfaces are extensive. We studied utility of positron emission tomography/computed tomography (PET/CT) tracer aluminium [^{18}F]fluoride-labelled 1,4,7-triazacyclononane-1,4,7-triacetic acid conjugated folate (Al[^{18}F]F–NOTA–Folate) targeting the FR-β receptor on activated macrophages for the assessment of inflammation in rats with MI. **Methods:** Surgical ligation of the left anterior descending (LAD) coronary artery irreversibly induced MI, while the sham model was prepared with similar procedures except ligation. Al[^{18}F]F–NOTA–Folate tracer was administered intravenously to perform PET studies at three different time points (3, 7 and 90 days post-MI) using *in vivo* PET/CT imaging and *ex vivo* digital autoradiography for both MI and sham groups. Additionally, rat heart cryosections were prepared for histological (hematoxylin-eosin) and immunohistochemical staining with anti-CD68 antibody detecting activated macrophages. Uptake of Al[^{18}F]F–NOTA–Folate was evaluated in the MI region and the remote area in both groups by image analysis. **Results:** In the MI model, infarcted cardiac areas had higher tracer uptake in *ex vivo* autoradiography compared to the remote areas or corresponding regions in sham-operated rats. Anti-CD68 immunohistochemistry demonstrated increased macrophage activity in the infarcted areas. The Al[^{18}F]F–NOTA–Folate uptake in the infarcted area and amount of CD68-positive cells correlated positively and significantly. **Conclusion:** The study suggests that the novel Al[^{18}F]F–NOTA–Folate PET tracer targeting FR-β expressed on activated macrophages is a promising tool for non-invasive imaging of inflammation associated with MI. Further research is required to clarify if this tracer is useful in the diagnostic and prognostic evaluation after MI.

KEYWORDS: Myocardial infarction, Positron emission tomography, Autoradiography, Inflammation, Folate receptor β, Al[^{18}F]F–NOTA–Folate

ABBREVIATIONS

[18F]FDG	2-Deoxy-2-[18F]-fluoro-*D*-glucose
^{18}F	Fluorine-18
Al[^{18}F]F–NOTA–Folate	Aluminium [^{18}F]fluoride-labelled 1,4,7-triazacyclononane-1,4,7-triacetic acid conjugated folate
ACD	Annihilation coincidence detection
ACE	Angiotensin converting enzyme
ARG	Autoradiography
CABG	Coronary artery bypass grafting
CHD	Coronary heart disease
CT	Computed tomography
cTn	Cardiac troponin
CVD	Cardiovascular disease
ECG	Electrocardiography
Echo	Echocardiography
FR	Folate receptor
FOLR2	Folate receptor 2
FR-α	Folate receptor alpha
FR-β	Folate receptor beta
FR-γ	Folate receptor gamma
FR-δ	Folate receptor delta
GPI	Glycosylphosphatidyl
H&E	Hematoxylin and eosin staining
HDL	High-density lipoprotein

HPLC	High-performance liquid chromatography
IHD	Ischemic heart disease
LDL	Low-density lipoproteins
MI	Myocardial infarction
PBS	Phosphate-buffered saline
PCI	Percutaneous coronary intervention
PET	Positron emission tomography
PSL	Photostimulated luminescence
ROI	Region of interest
TEE	Transesophageal echocardiography
TTE	Transthoracic echocardiography

TABLE OF CONTENTS

1. INTRODUCTION

The human body ceases to exist when the heart stops beating. This critical organ must be cared for so that it may continue pumping. Continuous blood flow to the coronary arteries is essential for the sustained cardiac function. Cardiovascular disease (CVD) is the leading cause of death in Europe and internationally and poses a significant economic burden on health systems. Meanwhile, the fatalities of ischemic heart disease (IHD) accounts for 45 percent in females and 39 percent in men across all European nations (Timmis et al., 2022). However, it is the utmost importance to develop non-invasive diagnostic approaches for coronary heart disease (CHD). One of the most important tools in the detection myocardial infarction (MI) is the imaging evidence of significant death of viable myocardium or detecting regional wall motion abnormalities. (Sagris et al., 2022).

Positron emission tomography (PET) offers detailed imaging of any physiological mechanisms, which is equally significant as morphological imaging obtained by other conventional methods. By viewing the decay of radionuclides attached to the molecules the molecular imaging can be obtained (Ollinger & Fessler, 1997). Autoradiography (ARG) is a technique to detect radionuclides that have been coupled to a specific target in tissue samples using a photo-emulsion layer or a radio-sensitive film. Because the samples contain radiotracers, it is possible to capture high-resolution images of the distribution of radioactivity in tissues in great detail (Fanchon et al., 2015; Johnston et al., 1990).

Since activated macrophages express folate receptor beta (FR-β), aluminum fluoride-18-labeled 1,4,7-triazacyclononane-1,4,7-triacetic acid conjugated folate (Al[^{18}F]F–NOTA–Folate) was investigated as a novel FR-targeting radiotracer for the imaging inflammation associated with MI in a rat model. *In vi*vo PET/computed tomography (CT) imaging, as well as *ex vivo* digital ARG were used to study the uptake of Al[^{18}F]F–NOTA–Folate. Association with macrophages was evaluated by immunostaining with anti-cluster of differentiation 68 (CD68) antibody. This study focused on the digital ARG imaging along

with immunostaining to find analytical evidence for increased activity of FR-targeted radiotracer in infarcted zones.

2. REVIEW OF THE LITERATURE

2.1 Myocardial Infarction

Myocardial injury can be detected by even minimally elevated level of cardiac troponin (cTn) found in a single measurement. In addition, if any clinical symptoms of myocardial ischemia, new electrocardiography (ECG) changes or imaging evidence or development of pathological Q wave in ECG or evidence of coronary thrombus by angiography are visible, it is considered as MI (Thygesen et al., 2018). The most common reason for MI is atherosclerosis, which can lead to athero-thrombosis. There are two primary categories of MI. Complete blockage of a coronary artery is considered an ST elevation MI (STEMI), while partial blockage or occlusion with collateral circulation is considered a non-ST elevation myocardial infarction (NSTEMI). The imbalance between supply and demand of oxygen leads to ischemic myocardial injury, i.e. MI. Changes in ECG and biomarkers are not always demonstrable. (Anderson & Morrow, 2017). cTn is the main biomarker for defining MI, although it has some limitations. It may remain elevated for prolonged periods, which may misdirect the follow-up prognosis of the disease. It is important to observe this life-threatening disease for a multitude of reasons, one of which is the possibility of reinfarction brought on by circulating emboli (Reed et al., 2017).

2.1.1 Epidemiology

CVD is the most common cause of mortality worldwide. Moreover, IHD is responsible for approximately half of the cases. Similarly 40 million people die due to CVD every year in Europe and 44% of them are due to IHD (N. Townsend et al., 2022). According to the World Health Statistics 2022, IHD carries the greatest risk of early mortality for women in more than one half of all nations, and it bears that risk for males in more than three quarters of all countries (World Health Organization, 2022). For the past four decades, life expectancy in the developed nations has been rising, but at the same time, the prevalence of IHD has been rising as a comorbid complication among the population. (Roger, 2007). This burden has transferred from nations with a high standard of living to those with a middle-class income or below. The incidence per 1000 people is 4.13 in low-income nations, 2.21 in middle income countries, and 1.92 in high income countries. The main reasons for the steady downward trend in the developed nations are the high preventative measures and the increased facilities for revascularization interventions (Anderson & Morrow, 2017). During the past two decades, these interventions have resulted in a 5-6% reduction in in-hospital mortality and a 7-18% reduction in 1-year post-STEMI death. Nonetheless, NSTEMI cases have grown dramatically and now account for 60-75% of all MI patients. Sudden cardiac death (SCD) refers to death within an hour of the onset of any cardiac symptoms. Patients who have had a STEMI or an NSTEMI have the highest incidence of sudden cardiac death, which accounts for roughly 30 percent of all mortality. The majority of SCDs occur in NSTEMI patients even after they have received appropriate therapy. Implantable cardioverter defibrillator (ICD) is recommended for those, whose ejection fraction is below 35%. It is also noted that the chances of death is higher in a period of one month after suffering from an acute event of MI (Koivunen et al., 2023).

2.1.2 Risk factors

Atherosclerotic lesion is one of the main culprits for development of MI. The formation and disruption of this lesion is a chronic inflammatory process fuelled by high cholesterol and low-density lipoprotein (LDL), reduced high-density lipoprotein (HDL) level, hypertension, smoking and diabetes mellitus (Rafieian-Kopaei et al., 2014). Although there are many non-modifiable risk factors like age, sex, race, environmental and genetic predisposition, we can remove other risk factors through changing dietary habit, avoiding alcohol intake and increasing physical activity (Koene et al., 2016). Several types of MI are defined depending on the specific underlying pathology. Coronary thrombosis is the most common cause of MI, followed by atherosclerosis that causes plaques to rupture or erode. The second kind occurs in the absence of acute atherothrombosis and is caused by an abrupt imbalance in oxygen supply or demand in the myocardium. SCD is linked to the third through fifth categories even in the absence of an elevated blood biomarker or revascularization treatments. Acute non-ischemic myocardial damage is a distinct kind of acute myocardial injury that is devoid of ischemia. Increases in cTn that persist over time indicate chronic myocardial damage. Moreover, different types of myocardial injury or MI require different acute treatment strategies due to basic biologic differences. Patients with the second kind have symptoms despite getting all preventative measures, whereas the first type is more common in young male patients who are unlikely to receive lipid lowering agents. As preventative use of lipid-lowering medicines has increased, new risk factors have emerged. Arterial rupture is quite uncommon today, according to a new study (DeFilippis et al., 2023; Reed et al., 2017). Cigarette smoking is a major contributor to cardiovascular disease worldwide. A history of smoking for a prolonged time was found in 64% of individuals with STEMI at their first presentation. Diabetes is the most rapidly increasing chronic disease, and its increasing incidence in this STEMI group reflects this upward trend. This rise is notable for both sexes. A STEMI patient with diabetes has a greater risk of death and higher chance of suffering from future cardiovascular complications than one without diabetes (Kazi et al., 2023). Platelet receptors are encoded by 4 different genes: *GP1BA, ITGB3, ITGA2*, and *P2RY12.* Around eight polymorphisms have been found in these MI-causing genes (Pina-Cabral et al., 2018; Sagris et al., 2022).

2.1.3 Pathophysiology

Acute MI are caused by coronary atherosclerosis and a thrombus in the lumen of an artery in more than 70% of cases. MI may also be led by coronary spasm, embolism, or thrombosis in healthy, nonatherosclerotic vessels (White & Chew, 2008). MI is another name for a heart attack, which occurs when the blood supply to the heart is suddenly cut off, causing damage to the heart muscle. When one of the coronary arteries supplying the heart with oxygen and nutrients, become clogged, the reason is often the rupture of an atherosclerotic plaque. Coronary arteries are located over the heart wall. In the pathophysiology of MI, there are a few mechanisms that are particularly significant. The formation of atherosclerotic plaques in the coronary arteries is the first step in the development of a MI. Plaques are the deposits made up of cholesterol, fatty streaks, and other substances that accumulate in the intimal layer of the artery walls. The greater the size of the plaque, the higher the probability that it may rupture (Frantz et al., 2022). When a plaque breaks, its contents are released into the circulation. These contents of plaques like cholesterol and other fatty compounds can lead to the formation of a blood clot at the site of the breach. As the plaque breaks, blood clots form at the site of the rupture. If the blood clots become large enough, they have the potential to completely block the coronary artery, so preventing blood from reaching the heart muscle. Ischemia is a condition that arises when the oxygen and nutrients needed by the heart muscle are unable to reach the muscle owing to a lack of blood flow. If the ischemia is severe and continues for a protracted period of time, the heart muscle may suffer infarction, which is the damage that cannot be reversed (Frantz et al., 2022; Leancă et al., 2022). Ischemia initiates a chain reaction of events, one of which is an inflammatory response. This response, in turn, attracts immune cells like macrophage and produces cytokines, all of which play a part in the destruction and remodelling of tissue. Scar tissue develops to replace damaged heart tissue, but this can have a detrimental effect on the ability of the heart to contract and pump blood. Scarring can occur after any type of cardiac injury. (Smit et al., 2020) The pathophysiology of a MI is influenced by a network of interconnected cellular and molecular processes. The severity of the damage and the patient's prognosis can be significantly improved with timely medical intervention, such as therapy with reperfusion to restore blood flow. In addition, prolonged cardiac arrest followed by resuscitation may cause global ischemia and reperfusion, which can lead to concentric subendocardial necrosis (Lambert et al., 2008). However, myocardial ischemia

leading to myocyte necrosis, causes inflammation, which depends on the length of the occlusion, the time between occlusion and reperfusion, and the presence of collateral circulation (Burke & Virmani, 2007).

2.1.4 Diagnostic Methods

Patients with MI have a propensity to develop left ventricular systolic dysfunction (LVSD). Most patients with MI have unidentified and untreated coronary artery disease, providing chances for commencement of evidence-based interventions with considerable potential to enhance clinical outcomes (Bularga et al., 2022). The cTn and the creatine kinase MB isoform are two widely used biomarkers for the diagnosis of acute MI. After permanent injury to the heart muscle, troponin leaks to the blood from necrotic myocytes. Elevation of troponin combined with a chest discomfort of patient or changes in ECG findings are diagnostic of MI. Clinicians may estimate the likely outcome of a heart attack based on the amount of cTn, which is directly proportional to the extent of the infarct. However, after reperfusion treatment, the washout effect might make the true troponin level deceptive. The maximum peak concentration of troponin occurs at 12 hours and persists for at least 10 days. Troponin has revolutionised the care of patients presenting with chest pain via its use in detecting AMI and risk stratification to facilitate decision making (Chan & Ng, 2010).

ECG is a tool for diagnosis that can record and analyse the electrical activity of the heart. This recording and analysis may be done in real time (Ducas et al., 2016). During a MI, alterations in the electrical activity of the heart can be observed by this device. The most familiar ECG changes are observed ST segment elevation or depression, pathological Q

wave and inversion of T wave (Saleh & Ambrose, 2018). ECG displays these characteristic patterns that are suggestive of myocardial ischemia or damage, which allows for a rapid diagnosis of infarction. Alterations to the ST segment or the appearance of Q waves on the electrocardiogram point to a problem in the area of the heart that is being affected. The ST segment of an ECG, which spans the period between the S wave's termination and the start of the T wave, should be at the same level as the baseline (Schmitt et al., 2001). When a patient has infarction, the ST segment frequently demonstrates either an elevation or a depression. On an ECG, Q waves are also crucial and can give extremely helpful insight. The appearance of Q waves on an ECG indicates that there is significant damage to the heart muscle. Q waves are not detected on a normal ECG (Sgarbossa et al., 1996). An ECG may not only diagnose the heart attack, but also it can determine the severity of heart attack. Besides, ECG is used to guide the treatment. In the event, that the electrocardiogram indicates that the infarction process is still ongoing, during that period more extreme measures may be required. Moreover, electrocardiogram is one of the many diagnostic tests that are used in the process of determining whether a patient has an infarction or not (Yusuf et al., 1984). The correlated clinical symptoms like pain or discomfort in the chest, shortness of breath, or nausea along with ECG changes indicate the most probable diagnosis of acute infarction, which needs an urgent medical intervention (Saleh & Ambrose, 2018).

Echocardiography (Echo) is a type of cardiac ultrasonography (US), which determines an abnormal heart wall motion and a decreased cardiac function or ejection fraction (EF). These help to diagnose MI. However, echo is non-specific and prone to error, as the experts are needed to perform the procedures and interpret the result (Panju, 1998). This is one of the popular non-invasive procedures, by which we can know the functional status of the heart. An echocardiogram is carried out by placing a transducer on the patient's chest or abdomen and then emitting the sound waves. These sound waves are allowed to bounce from the patient's heart, and this resulting echoes are utilised to create an image on a computer screen (Horowitz et al., 1982). The chambers, valves, and blood vessels of the heart can all be seen in this illustration, as well as providing the details of the anatomy and function of the heart overall. Echocardiograms can be performed in a variety of ways, including transesophageal echocardiography (TEE), transthoracic echocardiography (TTE), and stress echocardiography (Esmaeilzadeh & Parsaee, 2013). TTE is the method

that is performed the most frequently, because the transducer for the TTE is placed on the patient's chest. When doing a TEE, a flexible tube that is equipped with a transducer is placed into the oesophagus. This allows for the acquisition of an image of the heart that is more precise than what is achievable with a typical echocardiogram (Santoro et al., 1998). An echocardiogram may be conducted on a patient while they are excercising or during pharmacological stress to detect stress-induced ischemia. Echocardiography is able to identify a wide variety of cardiac conditions, including heart valve disease, congenital heart defects, cardiomyopathy, and heart failure. In addition to this, it can monitor how effectively a patient's treatment for heart disease is functioning (Mannaerts, 2004).

Computed tomography angiogram (also known as CTA) of coronary arteries is a diagnostic technique that provides images of the coronary arteries and the heart by using X-rays and a contrast dye. With its assistance, a diagnosis of MI can be made, and an evaluation of the extent of the damage to the heart muscle can be evaluated (Nikolaou et al., 2004). During a coronary CTA, a contrast dye is injected into blood vessels and then X-rays are taken at regular intervals to monitor the dye as it travels through the circulatory system of the body. It is possible that a narrowing or blockage of the blood flow to the heart muscle can be seen by the images of the coronary arteries (Nieman et al., 2006). An episode of heart attack is possible if there is a blockage that prevents blood from flowing to the heart. CTA has the additional capability of revealing the extent of damage to the cardiac muscle, in addition to determine the size and location of the infarction. With the use of these data, clinicians may also be able to make a more accurate evaluation to select the treatment modalities like introducing medication, angioplasty or stenting, or surgery, by which the patient may receive the best benefit (Hoffmann et al., 2009). The CTA offers an advantage over the other diagnostic procedures for heart disease in that it does not need the insertion of a catheter or any other devices into the body. On the other hand, there is an exposure to ionising radiation and the contrast dye might cause an allergic reaction. The findings of diagnostic tests, such as CTA, and a comprehensive clinical findings are used to diagnose MI and determine the appropriate course of treatment for this condition (The SCOT-HEART Investigators, 2018).

2.1.5 Management

The gold standard treatment of MI is primary percutaneous coronary intervention (PCI) which has to be done as soon as possible in the presence of an occluded coronary artery (possibly within 90 min or less, not more than 120 min) (Reed et al., 2017). If there is no option to perform PCI, thrombolytics should be administered immediately for life saving purpose. These drugs convert plasminogen to plasmin for dissolving the clot and opens the blocked artery to reperfuse the ischemic wall. The latest agents tissue plasminogen activators (alteplase, tenecteplase, reteplase) and PCI have the greater efficacy in reducing the mortality of MI. Medications like aspirin and nitro-glycerine are also introduced, and oxygen is administered to raise the oxygen level in the blood and alleviate chest discomfort and enhance blood flow to the heart. (Kunadian & Gibson, 2012). The primary objective of treatment is to increase blood flow to the portion of the heart that is compromised, thereby limiting myocardial damage.

Percutaneous coronary intervention (PCI) is performed when the vessels are clogged. A tiny tube or a catheter is inserted in that specific coronary arteries through a small incision in the groin or arm (femoral artery or radial artery cannulation) and steer it to the blocked spot. When the catheter reaches the narrowed spot, a tiny balloon is inflated to expand it, and a stent made of metal mesh is sometimes implanted to keep the artery open (Grech, 2003). When plaque builds up and narrows the coronary arteries, limiting blood flow to the heart muscle, is usually treated with PCI. Clinical correlation is also necessary to evaluate this treatment option is suitable or not. PCI has a low risk of complications and is often regarded as safe and effective. There is a chance of bleeding, infection, and artery or blood vessel damage, but this is true of every medical operation (Serruys et al., 2009).

Coronary artery bypass grafting (CABG) is another intervention that can be performed to repair coronary arteries that have been blocked or constricted. Coronary arteries are the channels that supply the heart muscle with oxygen and nourishment(Melly et al., 2018). During the operation, a surgeon removes a blood vessel (graft) from another location of the body, such as the chest, leg, or arm, and then use it to build a new pathway for blood to flow around the section of the coronary artery that is obstructed or restricted. This will allow blood to flow more freely (Green et al., 1968). Patients who have major blockages in many arteries or in parts of the heart that cannot be treated with PCI, such as those with heavily calcified or diffusely diseased arteries, are often candidates for CABG. This type of surgery is also indicated for patients who have diffusely diseased arteries and involving mainly the left main coronary artery. This coronary artery is the largest (Alexander & Smith, 2016). The CABG procedure is conducted under general anaesthesia, and patients must often stay in the hospital for several days after the procedure. There is a possibility of bleeding, infection, and injury to the heart, lungs, or other organs with this procedure, just as there is with any other type of surgery. CABG is usually regarded as a safe and successful operation, and many patients report a considerable improvement in their symptoms following the procedure However, there is a minimal chance of myocardial damage and coronary thrombosis during the procedures of PCI or CABG (Serruys et al., 2009).

Medications, such as beta blockers, angiotensin converting enzyme (ACE) inhibitors, and statins, to lower cholesterol levels, lessen their impact on the heart, and prevent future coronary artery disease (Reed et al., 2017). Modifications to a person's lifestyle, such as adopting a heart-healthy diet, engaging in regular exercise, giving up smoking, and learning to effectively manage stress, can help lower the risk of future heart attacks (Anderson & Morrow, 2017). Cardiac rehabilitation, which may involve supervised exercise, education on heart-healthy living, and counselling to help patients cope with the emotional burden of having suffered a previous episode of attack. These are provided to the patients in order to assist them in recovering from the effects of having suffered a heart attack (Burke & Virmani, 2007).

2.2 Macrophage

Macrophages have a crucial role in the onset and progression of MI. During MI, the heart undergoes a repair reaction that consists of three overlapping phases: the infarction phase, the inflammatory phase, and the proliferative phase (Lambert et al., 2008; Zhang et al., 2021). Damaged cardiomyocytes and neutrophils are migrated to the infarcted zone during the infarction phase, when they produce a plethora of inflammatory mediators that are crucial for the later inflammatory stage. This is the natural reaction of the body to any injury (Christia & Frangogiannis, 2013). The phagocytosis of dead cells, the removal of debris, and the production of growth factors, cytokines, and other substances that govern the healing process are all functions that macrophages execute following a MI. Two primary kinds of macrophages may be distinguished based on surface markers and functionality: classically activated M1 macrophage and alternatively activated M2 macrophage (Fadok et al., 1998; Martinez & Gordon, 2014). Tumor necrosis factor-alpha (TNF-α), interferon-gamma (IFN-γ), and lipopolysaccharide (LPS) all have a role in the activation of M1. The release of pro-inflammatory cytokines by activated M1 macrophages like interleukin-1 (IL-1), interleukin-6 (IL-6), interleukin-12 (IL-12), interleukin-23 (IL-23), inducible nitric oxide synthase (iNOS) and other cytokines and chemokines play a role in promoting inflammation, tissue damage, and adverse remodelling of the heart. Clearance of dead cells and cellular debris are facilitated by inflammatory cytokines, which are secreted by M1 macrophages and NK cells during the inflammatory stage (Martinez & Gordon, 2014). Tissue healing, collagen synthesis and cell multiplication culminate in the proliferative phase, where anti-inflammatory M2 macrophages produce cytokines. Stimulating interleukin-4 (IL-4), interleukin-13 (IL-13), and interleukin-21 (IL-21) results in the activation of M2 macrophages. In the subsequent phase, anti-inflammatory cytokines such interleukin-10 (IL-10) and transforming growth factor-β (TGF-β) and vascular endothelial growth factor (VEGF) are produced by M2 macrophages (Fadok et al., 1998). TGF- β and IL-10 may be able to stimulate myofibroblasts into generating collagen, while VEGF may induce cell proliferation and the formation of blood vessels (Shiraishi et al., 2016). Modulation of macrophages aids in the healing of injured myocardium by increasing angiogenesis and decreasing hypertrophy, fibrosis, and cell death (Mouton et al., 2018). On the other hand,

inflammation that is both severe and long-lasting can sometimes lead to abnormalities in cardiac remodelling and ultimately heart failure. As a consequence of this, there is significant therapeutic potential in the manipulation of macrophage activity for the imaging of MI (Cheng & Rong, 2018). Controlling macrophages in MI can be accomplished in a few different ways, including restricting monocyte recruitment, modifying the polarisation of macrophages, and boosting efferocytosis in macrophages (Zhang et al., 2021).

2.3 Folate Receptor Beta

Folate receptors (FR) are made up of four different glycopolypeptides: folate receptor alpha (FR-α), folate receptor beta (FR-β), folate receptor gamma (FR-γ), and folate receptor delta (FR-δ) (Kelemen, 2006). Among them, FR-α and FR-β have been the subject of a significant number of studies. Folate receptor β (FR-β) is a glycosylphosphatidyl (GPI)-anchored plasma membrane protein being expressed on myeloid lineage specifically on activated macrophages, but this is not the case in resting macrophages (Jager et al., 2014). It is also referred to as the folate receptor 2. (FOLR2). Macrophages have a strong attraction to folates, which is an important nutrient of our body system also. A significant affinity for folate is shown by the transmembrane protein FR- β. As a result, the feasibility of using imaging-based technique to study disorders mediated by macrophages has been explored on these folate receptors (Steinz et al., 2022; Warmink et al., 2022).

Placenta and hematopoietic cells are the only normal tissues that have considerable expression of FR-β, while all other tissues have no evidence of this protein. Recent research has shown that FR- β has also been identified in the synovial macrophages that are present patients suffering from rheumatoid arthritis and leukaemia (Elnakat, 2004; Ross et al., 1994). Physiologically, Folate is necessary for the formation and division of cells, and FR-β is an essential component in the process of its distribution. FR-β is able

to bind to folate to increase the amount of the folic acid that is absorbed by cells. In addition to its fundamental role in folate transport, FR-β has a role in a number of other biological processes (Elnakat, 2004).

2.4 Imaging Modalities

2.4.1 Positron Emission Tomography

Clinical PET is an imaging modality within nuclear medicine that has elevated the field to the forefront of patient care, particularly in Oncology, Cardiology and Neuropsychiatry. It can measure myocardial perfusion and viability, which are essential factor in the prognosis of any heart disease (Bailey, 2005). Accelerators and cyclotrons are nuclear reactors that may create radionuclides. The bombardment of stable nuclei is done by energy-rich protons. In nuclear reactions, several unstable nuclei are created. Produced radionuclides are proton-rich and decay through positron emission or electron capture. Positron produces PET imaging. Positrons are released by the disintegration of the tracer, and they travel a short distance before colliding with electrons in the tissue and being destroyed (Lameka et al., 2016). Two gamma rays are emitted 180 degrees apart from one another. These photons are detected by a network of ring detectors around the subject. When two or more detectors detect photons simultaneously, this is known as annihilation coincidence detection (ACD). The ACD is identified using scintillation detectors (Figure 1). If the annihilation happened near to the line joining the directions of two photons, a single detector ring will catch the photon, and the scanner's coincidence circuitry will identify the line in space along which the positron was destroyed. The information is saved in the computer, which creates transverse pictures using filtered back

projection. Finally, the slice of interest is rendered visually (Muehllehner & Karp, 2006; Raichle, n.d.).

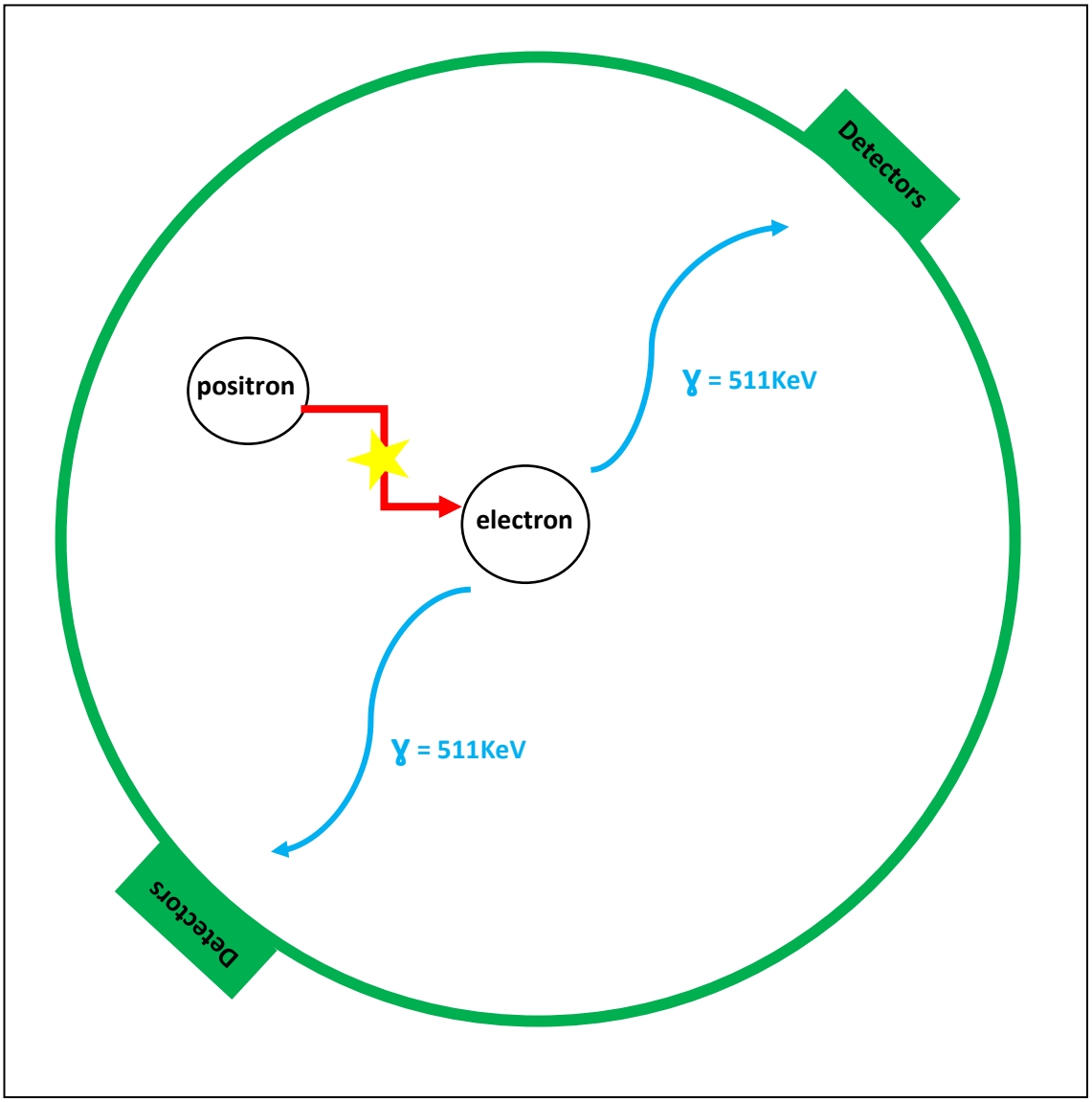

Figure 1. When a positron annihilates an electron in a particular tissue, the resulting gamma rays (511 KeV) can be collected up by scintillation detectors located in the PET scanner. *(KeV = kilo-electron-volt) Images are recreated from (Kim et al., 2013)*

PET investigations provide for an exceptionally fine level of visualisation of the body's internal organs and tissues. The ability to detect diseases and conditions at an earlier stage, when they are more curable, is one of the primary benefits of PET scans. PET scans are

commonly utilised in the staging process for cancer, which is critical for determining the course of the illness and formulating an efficient treatment approach. In addition to this, it may be used to monitor the effectiveness of treatments such as radiation and chemotherapy (Jin et al., 2022). This technique may also be applied in clinical trials and research inquiries to advance our understanding of diseases and the identification of feasible treatments. When it comes to medical imaging, PET scans are an extremely helpful tool that can diagnose and treat a wide range of diseases and conditions. The use of PET scans, on the other hand, should be examined on a case-by-case basis because, similar to other types of medical tests, they come with their own unique set of limitations and potential risks (Hegi-Johnson et al., 2022).

PET scans have the potential to provide both false positive and negative results. False positive results may result in testing or treatment that is not necessary, whilst false negative results may cause a delay in diagnosis and treatment. During a PET scan, a small amount of radioactive tracer is administered into the patient's body, and as a result, the patient may be subjected to radiation (Jiang et al., 2019). The patient's long-term risk of cancer may be increased as a result of radiation treatment; nevertheless, the doses used are far within the safe range. PET scans could come with a hefty price burden. If patients want to have a PET scan done, they might have to travel far away to a facilities that specialises in the procedure. It's possible that the subjects may be needed to abstain from medications and fast for many hours before getting a PET scan. It's possible that some individuals might experience an unfavourable reaction to the tracers used in PET scans (D. W. Townsend, 2008). Before PET scans are performed, a medical professional ought to thoroughly examine both the potential downsides and positive aspects of doing so, despite the fact that these scans have their applications. Before undergoing procedure, individuals should take certain precautions about any hazards (Kim et al., 2013).

2.4.2 Computed Tomography

CT scans take x-rays of a patient from several angles, which frequently shoot rays out in a fan or parallel direction to the patient's body, to provide a thorough image of the region of interest. The 2D data is then processed by a computer to generate numerous picture slices. Each 2D slice multiplied by its thickness generates 3D voxels, or cone beams, which, when assembled by computer processing, provide 3D representations of the scanned region of interest (Hampel, 2022).

CT scan is a type of medical imaging that uses computer technology along with X-rays to produce images of the body that are cut into cross-sections. The scanner consists of an X-ray tube, which generates a focused beam of X-rays, and a detector, which detects the radiation after it has passed through the body of a subject. Together, these two components allow the scanner to create three-dimensional images. The subject is placed in the core of a spinning gantry that also contains the X-ray source and detector (Fleischmann & Boas, 2011). The amount of X-rays that are absorbed by various regions of the body as the beam moves through the body is determined by the tissue density of those sections of the body. The density of the tissue that is being captured has a direct impact on the amount of attenuation, or weakening or loss in strength, that an X-ray beam experiences. More X-rays are absorbed by dense tissues, such as bones, than they are by soft tissues, such as muscles or organs. After passing through the body, the X-rays are picked up by the detector, which then converts the readings into electrical impulses. The information is gathered by the CT scanner and then sent to a computer for processing. The information is then put through a series of intricate computations on the computer, which result in the generation of cross-sectional images that are anatomically accurate. The attenuation of the X-rays at different locations in the body must be mathematically computed, and then the information is utilised to construct precise images of the internal structures. CT scan produces high-resolution, three-dimensional images of the human body. These images enable a medical professional to make an accurate diagnosis of a wide range of diseases and injuries (Cantatore & Müller, n.d.; Kalender, 2006).

CT scans are able to provide images that are extremely detailed, allowing for a more accurate diagnosis of medical issues than other imaging technologies. CT scans produce images of internal body structures and organs. Moreover, CT scans can be conducted in a matter of minutes and are reasonably speedy, because of that they enable medical professionals to quickly diagnose and treat a variety of medical conditions (Garvey, 2002). Unlike some other medical imaging procedures, CT scans are non-invasive and do not involve any incisions or introduction of tools into the body. This imaging modalities are an extremely helpful diagnostic tool for a broad variety of medical disorders. CT scans have the potential to be highly helpful in the early detection of cancer, which in turn enables earlier treatment and improves the patient's chances of recovery. It is widely agreed that CT scans are safe and have only a minimal threat of having unintended consequences (Smith-Bindman, 2010).

However, CT scan has some drawbacks also. Ionizing radiation emitting during scanning process has been linked to an increased likelihood of developing cancer. The quantity of radiation exposure received by the patient is determined by the type of scan performed, and also depends on the part of the region that is being scanned, as well as their age and gender (Withers et al., 2021). It is possible for some individuals to experience an allergic response to the contrast dye that is used in CT scans. The symptoms might range from something as simple as moderate itching and hives to something as severe as dyspnea. People who already have compromised renal function or who are given extremely high doses of the contrast dye that is used in some CT scans are at risk of experiencing kidney damage as a result of the dye. It is possible for some individuals to have feelings of anxiety or claustrophobia during a CT scan, particularly if they are required to remain in a confined space for a lengthy amount of time. CT scans may be rather expensive, and they can occasionally yield false positive findings (Brenner, 2007).

2.5 Digital Autoradiography

In the field of biomedical research, ARG is a method that is utilised to visualise the distribution of radioactive substances within tissues. It includes subjecting a sample of tissue or a biological specimen to a radioactive material, such as a radiolabelled molecule or a radioactive isotope, and then capturing the pattern of radiation generated by the sample using X-ray film or another imaging technology. ARG locates radionuclides in *ex vivo* and *in vitro* tissues. This experiment uses ARG using phosphor plates. Small barium fluorobromide and divalent europium generate a lattice of phosphor plates that trap electrons in bromine-free regions. Following ex vivo sectioning after PET imaging or in vitro incubation in the radiotracer, radioactive tissue is put near the phosphor plate for exposure. The tissue radiation ionises europium, releasing electrons into the bromine vacancies in the phosphor plate lattice. Electrons are liberated from vacancies by excitation with a laser beam in a scanner, and europium releases UV photons when it returns to its divalent ground state. UV photons are digitalized to display the radioactive source's location (Barthe et al., 2020; Fanchon et al., 2015).

ARG is a potent technique that may be utilised for the investigation of the distribution of molecules inside tissues, as well as for the visualisation of the effects of medications, poisons, or other agents on biological systems. The sample of tissue or biological specimen is subjected to a radioactive material that has been labelled with a radioactive tracer, such as a radioisotope or radiolabelled molecule. This allows the radioactive substance to be detected using the radioactive tracer. The tracer is absorbed by the cells in the sample, and it subsequently becomes a part of the biological molecules that are being investigated (Barthe et al., 2020; Zeissler et al., n.d.). The sample is then fixed and immersed in a medium that will give support for the sample throughout the future imaging process. This is done so that the sample can be imaged accurately. A piece of film or a radiation-sensitive detector is brought into contact with the sample before the analysis can begin. After that, the film or detector is subjected to the radiation that is released by the radioactive tracer that is contained within the sample. The images of the distribution of radiation released by the radioactive tracer in the sample is then produced by developing the film or detector. Nevertheless, the method has a few drawbacks, including

the risk of being exposed to radiation and the difficulty in accurately determining how much of a radioactive tracer is present in a given sample.(Fanchon et al., 2015; Lear et al., n.d.).

There are several similarities between phosphor screen technology and film autoradiography. Both involve storing energy using a sensitive region that must come into direct touch with the sample initially. The beta electrons' deposited energy is stored in the material's lattice flaws throughout this exposition phase. After this initial exposure, the images are revealed, either chemically for film or optically for a phosphor screen. There is no way to verify the present degree of exposition due to the fact that exposition and revelation are handled separately. Especially in preliminary studies where the degree of activity is uncertain, this often results in insufficient or excessive exposure. From a practical standpoint, this is a benefit since up to several hundred samples may be exposed in parallel and disclosed one at a time, with the revelation phase taking far less time than the exposition stage. Barium fluorobromide grains, which typically make up phosphor screens, have been shown to contain small amounts of divalent europium. Europium atoms play no direct role in the energy storage phenomena. Typically, bromine vacancies act as electron traps and contribute to the lattice defects. Electrons created when beta particles penetrate the sensitive layer and ionise europium atoms are then trapped in the vacancies in bromine. These snares are metastable states that can endure for long time, allowing for extended periods of exposure. In the case of ultraweak activity samples, where the mean time between ionisations is on the order of the lifespan of the metastable state, there is a limit on how long one may expose the material to radiation. When this happens, the signal is no longer linear in terms of activity or exposition time, and the screen tends to lose as many charges as it creates (Bäck & Jacobsson, 2010; Fichet et al., 2012; Johnston et al., 1990).

The density of bromine vacancies and the density of europium atoms are closely connected to the quality of the phosphor screen. For instance, if there is an abnormally high density of vacancies, the lifespan of electron traps tends to diminish, and the sensitivity lowers because of the increased rate of recombination of electrons with ions. The picture on a phosphor screen can only be seen when europium ions have been introduced. This breakthrough is no longer chemical, but rather optical. Exposed light

causes the phosphor screen's trapped electrons to be released into the conduction band, where they will remain until they collide with an ionised atom of europium. Next, the electron and europium recombine, and the latter transitions back to its ground state while giving off a UV-blue photon. Screen features like grain size in a phosphor screen and overall thickness of a sensitive layer have just as much of an impact on spatial performance as the scanning device itself. Optical fibres or a lens focused on the laser dot gather the UV light, which is then converted into a digital signal on a photomultiplier. (Fichet et al., 2012; Johnston et al., 1990; Lear et al., n.d.)

2.6 Al[^{18}F]F–NOTA–Folate

Aluminum18F-labeled1,4,7-triazacyclononane-N,N′,N″-triacetic acid conjugated folate (Al[^{18}F]F–NOTA–Folate) is a PET tracer targeting folate receptor beta. It is labelled with ^{18}F (Figure 2). Although a number of other radionuclides have been used effectively in PET imaging, ^{18}F is often chosen as the radionuclide of choice due to the fact that it has optimal physical properties. It has a physical half-life that is reasonably lengthy (109.8 minutes), which makes it possible for ^{18}F-labelled tracers to be distributed to clinics after centralised synthesis. It has the perfect amount of positron energy, with a maximum energy of 0.635 MeV and an average of 0.25 MeV. Because of its high likelihood of β +

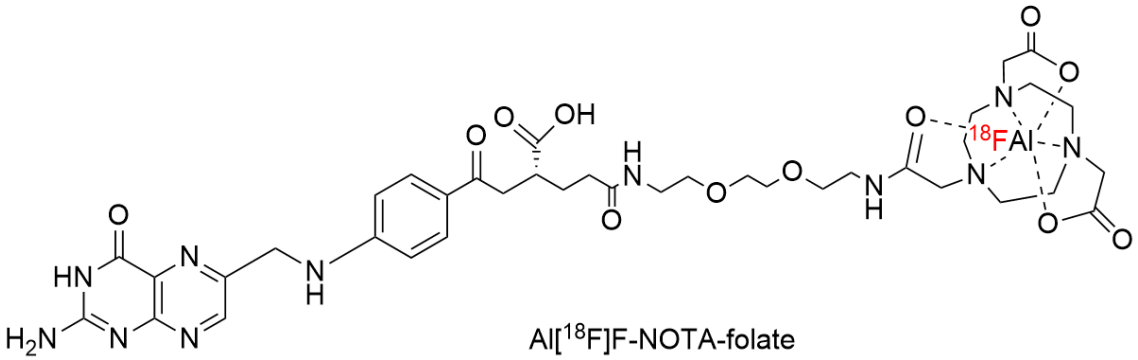

Figure 2. Structure of PET tracer

Aluminium^{18}F-labeled1,4,7-triazacyclononane-N,N′,N″-triacetic acid conjugated folate

emission (97%) and relatively low tissue energy deposition, it is capable of producing high-resolution pictures.

New FR-targeted PET tracers with faster preparation times, higher radiochemical yields, or increased specific activity are needed, despite the fact that numerous ^{18}F-labeled FR-targeted PET agents have previously been synthesized and evaluated in preclinical trials. That's why our interest to perform our pre-clinical study in the field of FR-targeted PET imaging (Chen et al., 2016).

2.7 Immunostaining

Immunostaining is used in the search for antigens in cells and tissues, including amino acids, proteins, infectious agents, and particular among cellular populations. The method consists of two parts, including preparation of the slides and stages of the reaction, as well as interpretation and quantification of the acquired expression. It is a vital tool for scientific study, as well as a complementary method for elucidating differential diagnoses that cannot be determined by traditional H&E staining (De Matos et al., 2010). Here we will use anti CD68 antibody and anti-FR-β antibody for immunostaining or receptor of interest on macrophage.

Immunostaining is a method that is performed to identify particular proteins or other molecules that are located inside of cells or tissues. Utilizing antibodies that are able to attach selectively to the molecule of interest and then utilising a variety of techniques to see the location of the antibody are both required steps in this process (Richter et al., 1999). In order for staining to be successful, the cells or tissue slices need to be appropriately prepared. Fixing the cells or tissue to preserve them and permeabilizing the cells to enable antibodies access to the components found inside the cells are both the leading steps in this process (Suthipintawong et al., 1996). It is necessary to block the sample with a protein solution, which is commonly produced from animal serum. This

will prevent the antibodies from attaching in a manner that is not specific to the target. The sample is given the opportunity to attach to the target, after which a primary antibody is added to the mixture. This antibody has been shown to selectively bind to the molecule of interest. Primary antibodies can be either monoclonal or polyclonal in nature, and for purposes of detection, they can be attached to either a fluorescent or an enzymatic label. The main antibody is followed by the addition of a secondary antibody that is specific to the primary antibody. This secondary antibody is frequently attached to a label like dye or enzyme, that may be used to visualise the position of the primary antibody in the sample. This allows the location of the primary antibody to be identified. Depending on the type of label that was used, the secondary antibody that was labelled can be detected utilising a variety of different methods (Ribichini et al., 2006; Richter et al., 1999; Suthipintawong et al., 1996). Immunostaining is a useful technique that allows one to see certain proteins or other molecules within cells or tissues, which can then be used to examine how they are distributed and where they are located (Piña et al., 2022).

3. AIMS AND HYPOTHESES

I) The first aim of the project was evaluation of the uptake of FR-β targeting PET tracer Al[^{18}F]F–NOTA–Folate in a rat model of MI using *ex vivo* digital ARG and immunostaining.

II) The second aim of this project was the biological evaluation of Al[^{18}F]F–NOTA–Folate tracers in MI rat model and the sham-operated rat model at three different time points through *ex vivo* digital ARG. Our hypothesis was that the tracer uptake is increased in the infarcted regions. The activity of radiotracer should show little to no activity in the remote area in case of MI model and all regions of the heart wall in case of sham rat model.

III) To prove the colocalization of macrophages and Al[^{18}F]F–NOTA–Folate, immunostaining was done with anti-CD68.

4. MATERIALS AND METHODS

4.1 Radiosynthesis of Al[^{18}F]F–NOTA–Folate

According to the standard protocol, the radiotracer Al[^{18}F]F–NOTA–Folate was synthesized upon the basis of procedure radiolabelling with Al[^{18}F]F, The time period for the total procedure was 77-88 min followed by the bombardment. It began with an incubation step including aluminium chloride ($AlCl_3$) and [^{18}F]-fluoride. The ingredients were then subjected to a 100°C heating process while NOTA-folate was added. In order to identify the radiolysis product, a high-performance liquid chromatography (HPLC) test was carried out. Phosphate-buffer saline (PBS; pH 7.4) was used as the medium for the incorporation of ^{18}F-FOL. This medium included 8% ethanol and 4–7% polypropylene glycol. Even after a total of four hours of radiosynthesis, radiolysis products were unidentified. The purity of the radiochemical was maintained over 95% and molar activity was 52 ± 22 MBq/nmol (n = 6).

4.2 Surgical Intervention to Prepare Rat MI Model

Before commencing the surgery, the operative area as well as all surgical tools were sterilised properly. We used glass bead sterilizer (Agntho's AB, Sweden) for sterilizing before each experiment. The heating pad of the rat was kept at a constant $37^0 \pm 1^0$C. Body temperature also has a role in determining the severity of an infarction. Prior to the surgery, the rats underwent a series of checks, including a visual examination, heart rate monitoring, temperature, and weight monitoring. If everything was uneventful, the rats were proceeded to surgery. Firstly, buprenorphine (Bupaq Multidose vet 0.3mg/ml,

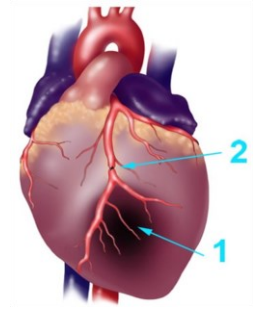

Figure 3. (1) Infarcted area in the myocardium, (2) location of ligation by suturing in left anterior descending artery

Richter Pharma) 0.04 mg/kg was injected subcutaneously before surgery and subsequently every 8 hours up to the 3rd post-operative day as an analgesic. We administered carprofen 5 mg/kg (Rimadyl vet 50mg/ml, Zoetis Finland Oy) and midazolam 1 mg/kg (Midazolam-Hameln 5 mg/ml, Hameln Pharma) subcutaneously as pre-anaesthetic medications. After 10 minutes, we induced anaesthesia by giving ketamine 45 mg/kg (Ketaminol vet 50 mg/ml, MSD Animal Health) and medetomidine 0.25 mg/kg (Cepetor vet 1 mg/ml, Vetmedic) intraperitoneally. The surgical region was prepared by first shaving the rat completely from the neck down to the chest, and then we disinfected the area with povidone iodine (Betadine 75 mg/ml, Takeda Oy) and 70% ethanol solution. Finally, lidocaine 7 mg/kg (Lidocaine 10 mg/kg, Richmond Vet Pharma) was injected subcutaneously at the surgical site to relieve any discomfort. After that the rat was intubated and connected to a mechanical ventilator. The left ventricle was exposed first, therefore an incision was made at the left 4th inter-coastal gap. Then the ribs were stretched using a chest retractor. Isolating and ligating the left anterior descending artery (LAD) resulted in an infarction throughout the anterior wall of the heart (Figure 3). Myocardial tissue blenching proximal to the suture or malfunction of the anterior wall was an indicator for successful LAD ligation. For the sham-controlled rat, all the procedures were the same except that the LAD was not ligated. After the operation, air was evacuated from the chest cavity by using a sterile syringe and the chest wall was closed by suture. Then we administered Atipamezol hydrochloride 1 mg/kg (Antisedan Vet 5 mg/ml, Orion Pharma) for reversing anaesthesia. The rat's temperature and other vitals were monitored before it was placed in a cage to rest and recuperate.

4.3 In Vivo PET/CT Imaging

Total 32 rats were scanned and sacrificed for organ collection. Animals were scanned 3 days, 7 days and 90 days post-MI. For the Day-3 study, 7 rats from LAD group and 6 rats from sham group were scanned. Similar scans were performed on 4 LAD ligated rats and 5 sham rats after 7 days, and on 6 LAD ligated rats and 4 sham rats after 90 days post-operation. Inveon Multimodality small animal PET/CT scanner (Siemens Medical Solutions, Knoxville, TN, USA) was used for *in vivo* PET/CT imaging. On the first session, a dynamic PET/CT scan was performed with [^{18}F]FDG to detect functional compatibility. On the following days, we performed PET scan with Al[^{18}F]F–NOTA–Folate tracers, which was injected through the tail vein of the rats. A 60-min dynamic PET acquisition and a 10-min static PET acquisition starting 30 min after injection was performed under isoflurane (Attane vet 1000 mg/g, Vet Medic Animal Health Oy) anaesthesia. Before beginning the PET imaging, a CT scan lasting ten minutes was carried out for the purpose of obtaining anatomical references and correcting attenuation. At 60 minutes after the radiotracer injection, the rats were euthanized, and their organs were extracted in pre-weighted test-tubes in order to measure their weights by measuring scale and radioactivity by using a gamma counter. The hearts underwent histopathological and immunohistochemistry staining as well as ARG analysis after being transported to the Histocore faciility in Medisiina D.

4.4 Ex Vivo Digital Autoradiography

After performing the PET scan with Al[^{18}F]F–NOTA–Folate tracers, the rat hearts were processed by the histocore department situated in Medisiina D, University of Turku for digital autoradiography (ARG) film plate (Fujifilm, Tokyo, Japan) preparation. 20µm and 8µm cryosections of heart was prepared and preserved at -70^{0} C for further Hematoxylin and Eosin (H&E) staining and CD-68 staining. After exposure time (approximately 4 hours) the plates was scanned by Fuji Film BAS-5000 scanner (Fuji Tokyo, Japan) in

Medisiina C. the images were saved as digital image in .inf and .img formats. Later on the images were processed by by Aida Image Analyzer v.4.50 (Raytest Isotopenmeßgeräte GmbH).

4.5 Hematoxylin-Eosin Staining

The preserved slides were sent to histocore department situated in Medisiina D, University of Turku for Hematoxylin and Eosin staining. 4 slides comprising 20 µm cryosections of heart were used for staining. As the sections were cut transversely, we used different horizontal levels of tissue sections to investigate all regions of infarction. Then the stained slides were scanned by Pannoramic 1000 scanner (3DHistec Ltd., Budapest, Hungary) to prepare digital images for further image analysis.

4.6 Immunohistochemical CD68 Staining

The slides were preserved at -70^0 C in a freezer, from where those were sent to histocore department situated in Medisiina D, University of Turku for CD-68 staining. Around 10 to 12 sections of two slides of each rat were used for this purpose. We employed various horizontal levels of tissue slices to study all locations of infarction since the sections were cut transversely. Then the stained slides were scanned by Pannoramic 1000 scanner

(3DHistec Ltd., Budapest, Hungary) to prepare digital images for further image analysis. This will specify the presence of activated macrophage in the inflamed myocardium.

4.7 Autoradiography Image Analysis

Digital ARG images was pre-prepared by Aida Image Analyzer v.4.50 (Raytest Isotopenmeßgeräte GmbH). Then Pannoramic Viewer (3DHistec Ltd., Budapest, Hungary) was used to set the magnification of 1:64 for H&E images, which was opened by GIMP 2.2 (www.gimp.org) later on to draw the regions of interest (ROIs). Subsequently, the ROIs of H&E images was superimposed over ARG images to draw the contours. After that, contours were redrawn over ARG images using TINA (Ravtest Isotopemessgeräte, GmbH, Straubenhardt, Germany) software, which gave us the radioactivity of ROIs in photostimulated luminescence per square millimetre, or PSL/mm^2. The data was then be exported to Microsoft Excel Worksheet (Microsoft Office 365, 2022) for statistical analysis. We drew ROIs that covered the whole infarcted zone of a section in the LAD-ligated rat. Another ROI was drawn in the distant area over the posterior or medial wall. In the instance of the sham-operated rat, we drew one ROI over the anterior wall and another ROI over the medial or posterior wall that was identical to the LAD group. ARG analysis was performed on slides 1, 2, 13, and 14. We examined four sections from slides 1 and 2, which included the basal and midzones of the heart. Moreover, we examined about two portions from each slide in the apical zone (slide no 13 and 14). We have ignored the fibrotic region and considered just the infarcted one in case of Day-90 time point. We also draw ROIs in sham group devoid of injured area. Additionally, while drawing the ROIs we avoided the papillary muscle and focused over the myocardium.

4.8 Image Analysis of CD68 Staining

The CD68 stained slides was analysed firstly by using Pannoramic Viewer (3DHistec Ltd., Budapest, Hungary) and GIMP 2.2 (www.gimp.org). For this purpose, we selected slides 10 and 22. Slide 10 had sections around the basal area, whereas slide 22 had sections from the apical zone. We separated the infarcted part and a region of a remote area (medial and posterior wall) from the sections of LAD group. Similarly, from the sham group, we removed areas of the anterior wall and some of the medial and posterior walls. Then the processed parts underwent through image deconvolution plugin of Fiji, National Institutes of Health, U.S. This plugin calculated both stained and unstained area of the myocardium in pixel value. We also avoided the papillary muscle and injured muscle or pericardium of sham-operated group.

4.9 Experimental Animals

Adult male rats of the Sprague-Dawley strain that are 8 to 10 weeks old and weigh between 250 and 450 grams were utilised for the experiment. A total number of 32 rats were used for the experiment. The animals were housed in The Central Animal Laboratory, University of Turku, Turku, Finland. The temperature was regulated between 18 and 24 degrees Celsius, while the relative humidity was controlled between 40% and 70%. The air in the room was changed around 10–15 times per hour, and the rats were housed in vented cages (IVC, Techniplast, Buguggiate, Italy). In these cages, the air was changed approximately 70 times an hour, where the rats were inlaid with autoclaved aspen chips (Tapvei Ltd, Harjumaa, Estonia). The RM3 (E) Soya Free diet (Special Diets Services, Essex, UK) and autoclaved tap water from the public supply (Turun vesilaitos, Turku, Finland) were given to the rats as their sources of nutrition. In this study, three scans were performed at predetermined intervals. There were 7 (n = 7) LAD ligated MI and 6 (n = 6) sham-operated control rat models for the Day 3 time point. During the Day 7 time point, there were 4 (n = 4) rats in the LAD group and 5 (n = 5) rats in the sham

group; and at the Day 90 time point, there were 6 (n = 6) rats in the LAD group and 4 (n = 4) rats in the sham group (Figure 4). All experiments on animals were performed in compliance with the applicable European Union regulation and with the approval of the national Project Authorization Board in Finland and carried out in compliance with the European Union Directive 2010/EU/63 on the protection of animals used for scientific purposes.

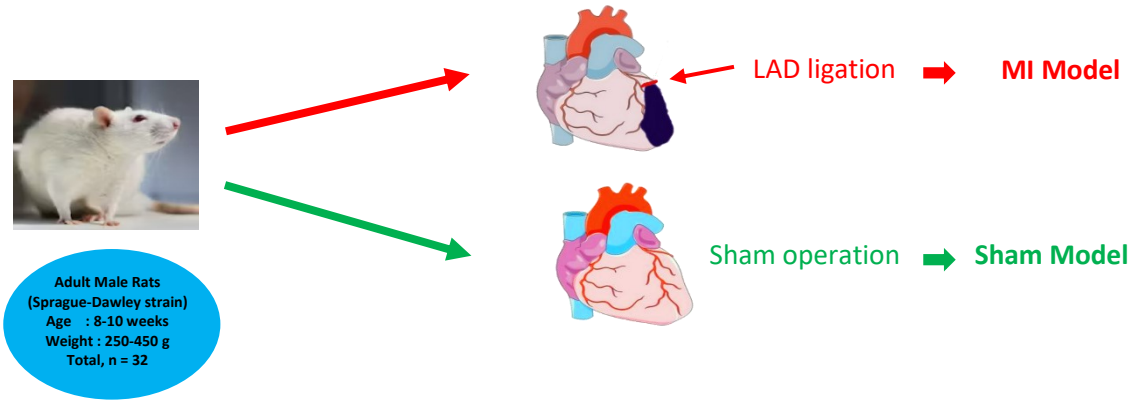

Post-operation days → **3 days** → **7 days** → **90 days**

Total number (n) of rats used in the experiment						
MI Model	**n = 7**		**n = 4**		**n = 6**	
Sham Model	**n = 6**		**n = 5**		**n = 4**	
	MI	**Sham**	**MI**	**Sham**	**MI**	**Sham**
H & E staining	n = 7	n = 6	n = 4	n = 5	n = 6	n = 4
Digital Autoradiography	n = 7	n = 6	n = 4	n = 5	n = 6	n = 4
Anti-CD68 staining	n = 7	n = 6	n = 4	n = 5	n = 6	n = 4
Total number of sections used for image analysis						
	MI	**Sham**	**MI**	**Sham**	**MI**	**Sham**
H & E staining images	80	60	44	61	71	50
Digital Autoradiography images	80	60	44	61	71	50
Anti-CD68 staining images	43	28	21	26	30	21

Figure 4. Study flow chart, (*figures are recreated from www.unil.ch and www.genetargeting.com)*

4.10 Statistical Analysis

The data was shown as a mean value and standard deviations. In order to compare normally distributed data, student's t testing was used. The statistical analysis was performed using Microsoft Excel Worksheet (Microsoft Office 365, 2022), with the significance level set at a *P* value of less than 0.05. After analysing the digital ARG images, infarcted region of both LAD and sham group was compared with two tailed student's t test. Besides, the remote zone of both group in a specific time point was also compared with same test. Then the *P* values were obtained. Additionally, the data gathered from infarcted area of both LAD and sham models in CD68 stained images were analysed by the same two tailed student's t test. Remote regions were analysed separately. Data from a particular time points were considered separately.

After gathering all data from infarcted region of all LAD groups from all time points in both digital ARG images and CD68 stained images were correlated with Pearson's correlation test. This correlation test was performed in IBM SPSS Statistics (version 29.0; IBM Corp.). Positive *R* value was considered as positive correlation. Similarly, as before mentioned, *P* value less than 0.05 was considered as significant. The correlation between all the three time points of ARG analysis and CD68 staining analysis were compared by using ANOVA test through GraphPad Prism version 9.5.1, where positive *F* value determined positive correlation and *P* value of less than 0.05 indicated significance. Tukey's multiple comparison test was also done to compare the paired relation between two timepoints where the significance level also adjusted at a *P* value of less than 0.05. This comparison tests were also performed in GraphPad Prism version 9.5.1. All graphs and tests were presented with the same GraphPad Prism version 9.5.1.

5. Results

5.1 Visual Uptake of Al[^{18}F]F–NOTA–Folate

We found that uptake of FR-β targeting PET tracer Al[^{18}F]F–NOTA–Folate was increased in infarcted myocardium. This was observed in different imaging modalities employed in this experiment. The digital ARG images of the LAD group showed clear uptake of the tracer over the infarcted area of the heart sections. This was visually identifiable when the H&E-stained slides were compared. The remote zones specifically over the medial and posterior wall of the heart showed minimal uptake of the tracer. These features were seen over all time points (Figure 5).

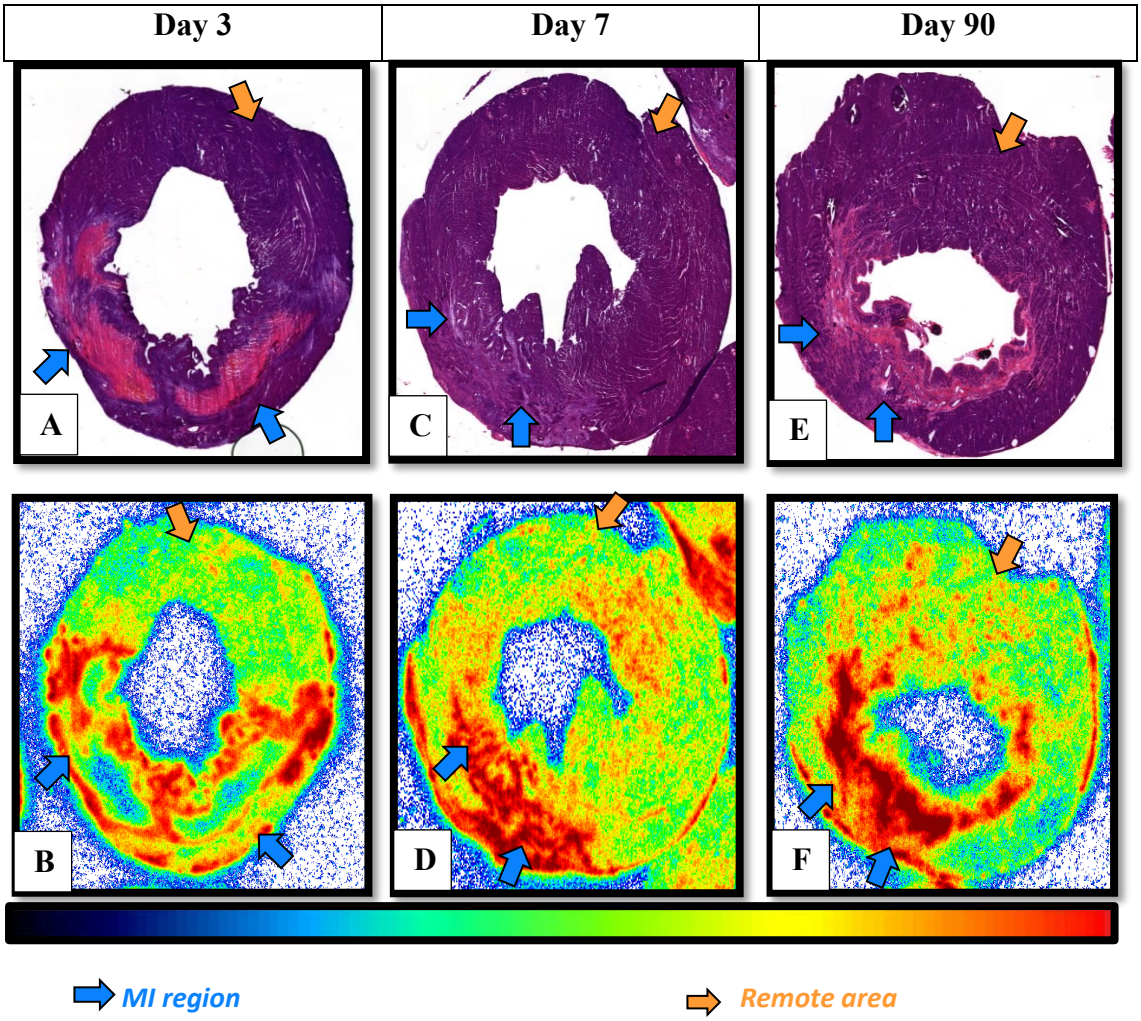

Figure 5. A) H&E images of LAD group showing MI region and remote area 3 days after LAD ligation; B) ARG images of corresponding section of A showing uptake of Al[^{18}F]F–NOTA–Folate along the MI region; C) and D) H&E images and corresponding

ARG images of LAD group showing MI region and remote area 7 days after LAD ligation; E) and F) H&E images and corresponding ARG sections of LAD group at Day 90 time point.

In case of the sham operated rats, the heart sections showed similarly minimal uptake of the radiotracer over all areas of the heart. Moreover, the images had obtained at 3 distinct time-points showed the same distinguishable findings visually. (Figure 6)

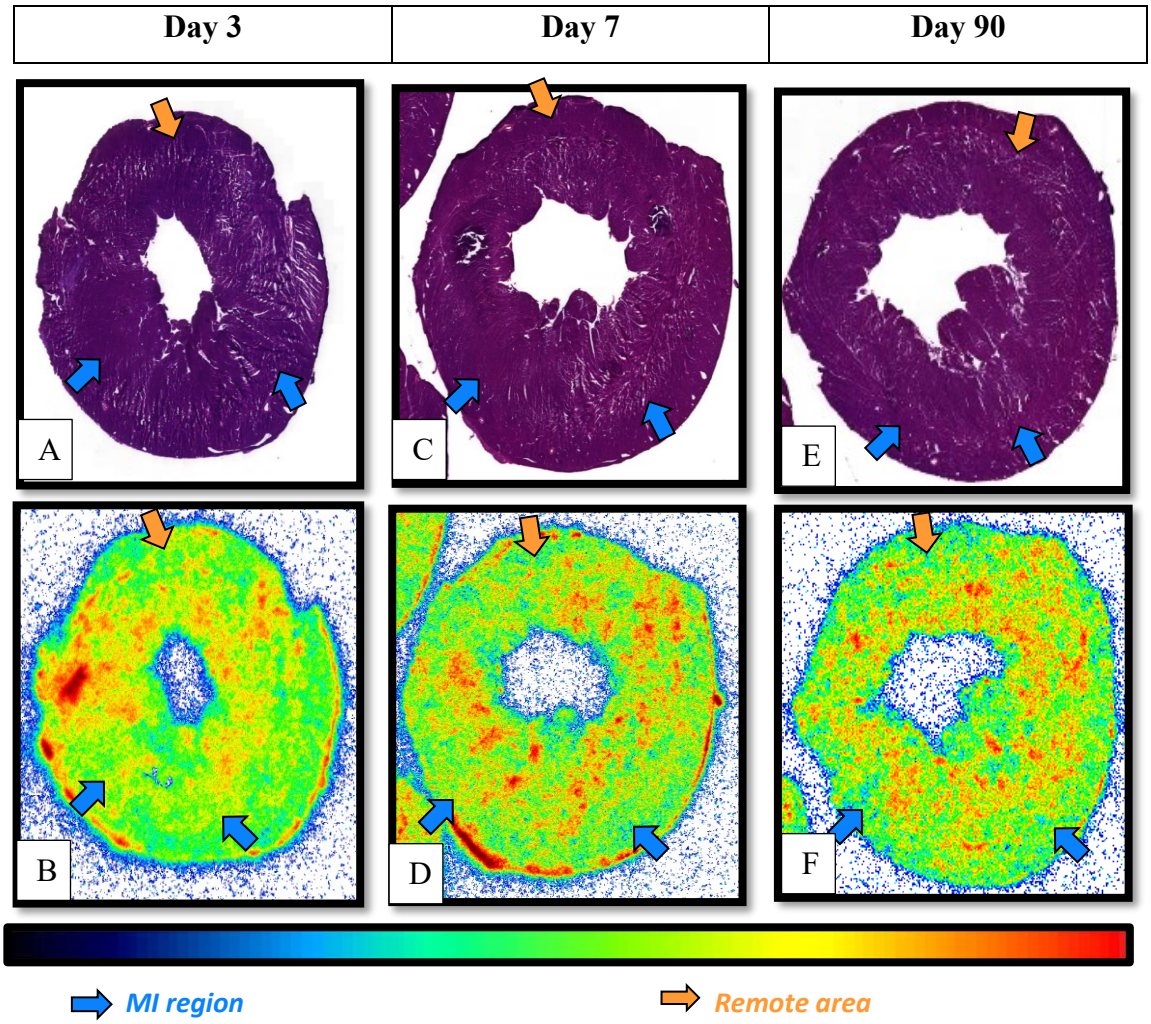

Figure 6. A) H&E images of sham group showing MI region and remote area 3 days after sham operation; B) ARG images of corresponding section of A showing no to low uptake of Al[^{18}F]F–NOTA–Folate along the MI region; C) and D) H&E images and corresponding ARG images of sham group showing MI region and remote area 7 days after LAD ligation; E) and F) H&E images and corresponding ARG sections of sham group at Day 90 time point.

Images stained with CD68 revealed positive staining in myocardial regions that showed uptake of Al[^{18}F]F–NOTA–Folate, as they related to the digital ARG images. The infarcted regions of the LAD group showed positive CD68 staining (Figure 7). However, the remote zones of the LAD group were remained unstained.

.

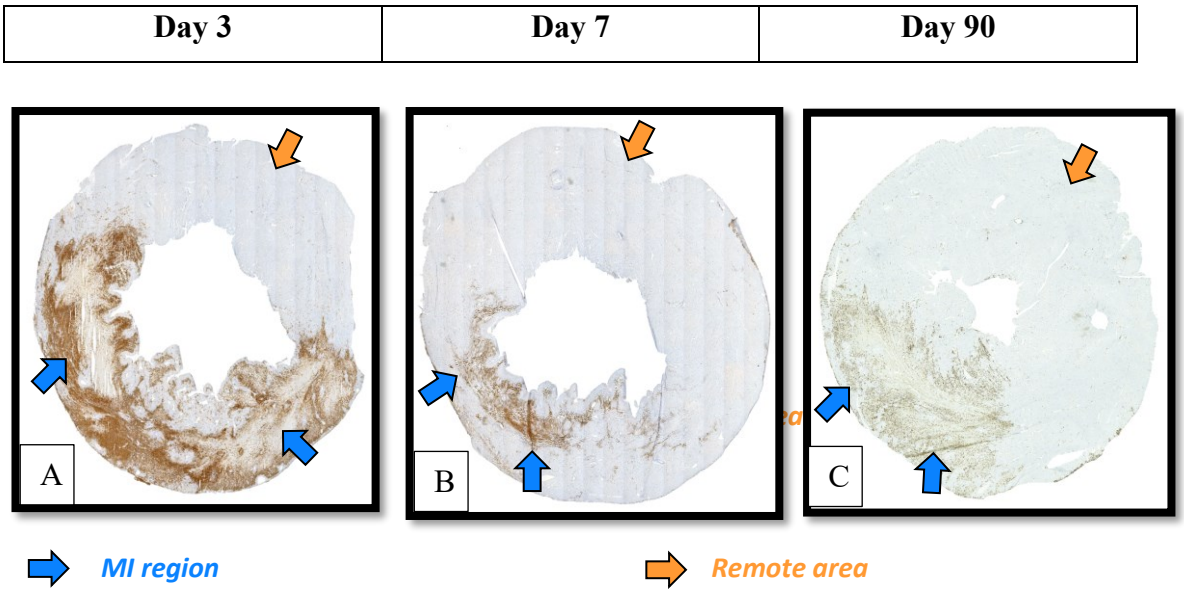

Figure 7. A) CD68 stained images of LAD group showing MI region and remote area 3 days after LAD ligation; B) 7 days after LAD ligation, CD68-stained images of the LAD group reveal the MI region took higher staining than the remote area.; C) CD68 stained sections of LAD group at 90 days timepoint.

Moreover, all areas of the sham group showed no positive staining. It was not distinguished even zooming in the images (Figure 8).

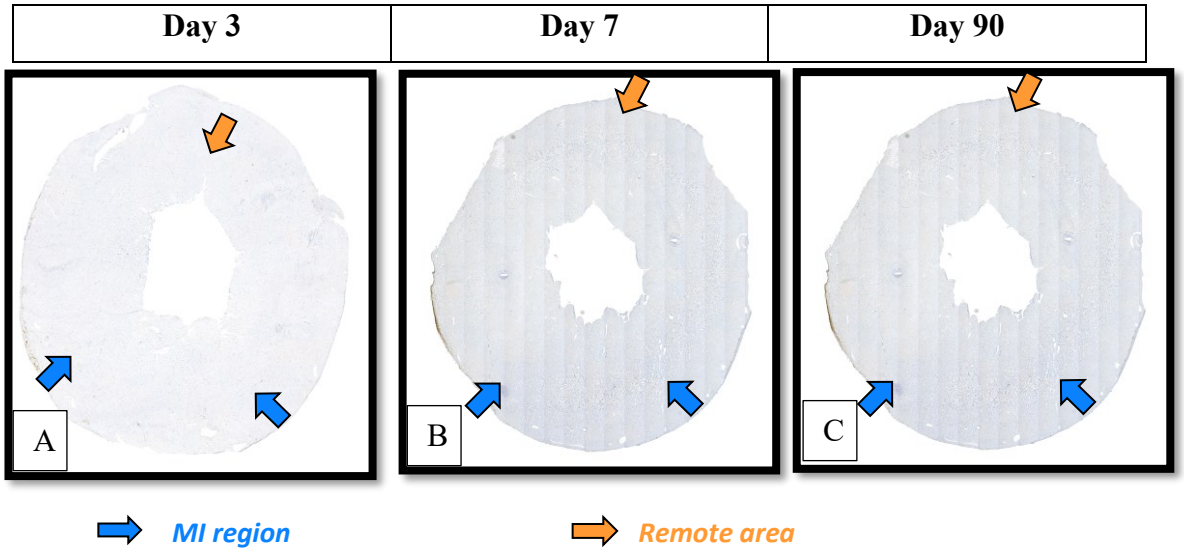

Figure 8: A) CD68 stained images of sham group showing MI region and remote area 3 days after sham-operation; B) 7 days after operation, CD68-stained images of the sham group reveal the both the MI region and the remote area have minimal staining; C) CD68 stained sections of sham group at Day 90 time point.

5.2 Ex Vivo Digital Autoradiography

The digital ARG images of the heart sections were analysed to find the uptake of Al[^{18}F]F–NOTA–Folate along the different regions of heart wall. The radioactivity of the infarcted zone and the remote areas of the LAD groups were evaluated. For the sham-operated rats the uptake of tracer along the infarcted areas (antero-lateral wall) was also assessed and compared with the remote areas. Furthermore, both the infarcted zones and the remote areas from both LAD and sham groups were analysed statistically to obtain *P* value.

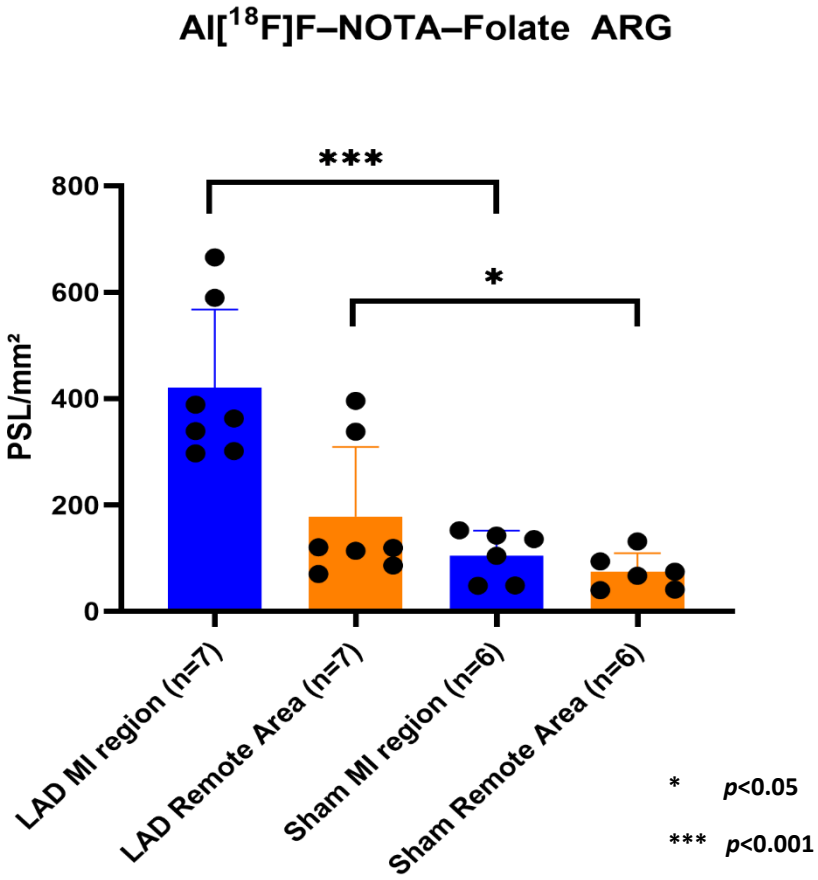

.

Figure 9. Autoradiography analysis 3 days after operation

At 3-day post-MI, the binding of Al[^{18}F]F–NOTA–Folate along the infarcted zones of the LAD group was expressed in PSL/mm^2 values, with an average value of 420.70 ± 135.81

PSL/mm^2 (n = 7). By contrast, the infarcted regions of sham group showed an average value of 105.37 ± 42.80 PSL/mm^2 (n = 6), with a *P* value of 0.0004. In addition, the remote areas of both LAD and sham group showed an average lower uptake of Al[^{18}F]F–NOTA–Folate (177.70 ± 121.79 PSL/mm^2 , n = 7 vs. 74.81 ± 31.62 PSL/mm^2 , n = 6; *P* = 0.091) (Figure 9).

Seven days after MI, the Al[^{18}F]F–NOTA–Folate binding was quantified over the infarcted zones of the LAD group, and the average value of this expression was found to be 279.87 ± 89.72 PSL/mm^2 (n = 4). In contrast, the identical region in the sham group exhibited an average uptake of 90.86 ± 23.10 PSL/mm^2 (n = 5), yielding a statistically significant *P* value of 0.005. Furthermore, it was observed that the remote regions of both

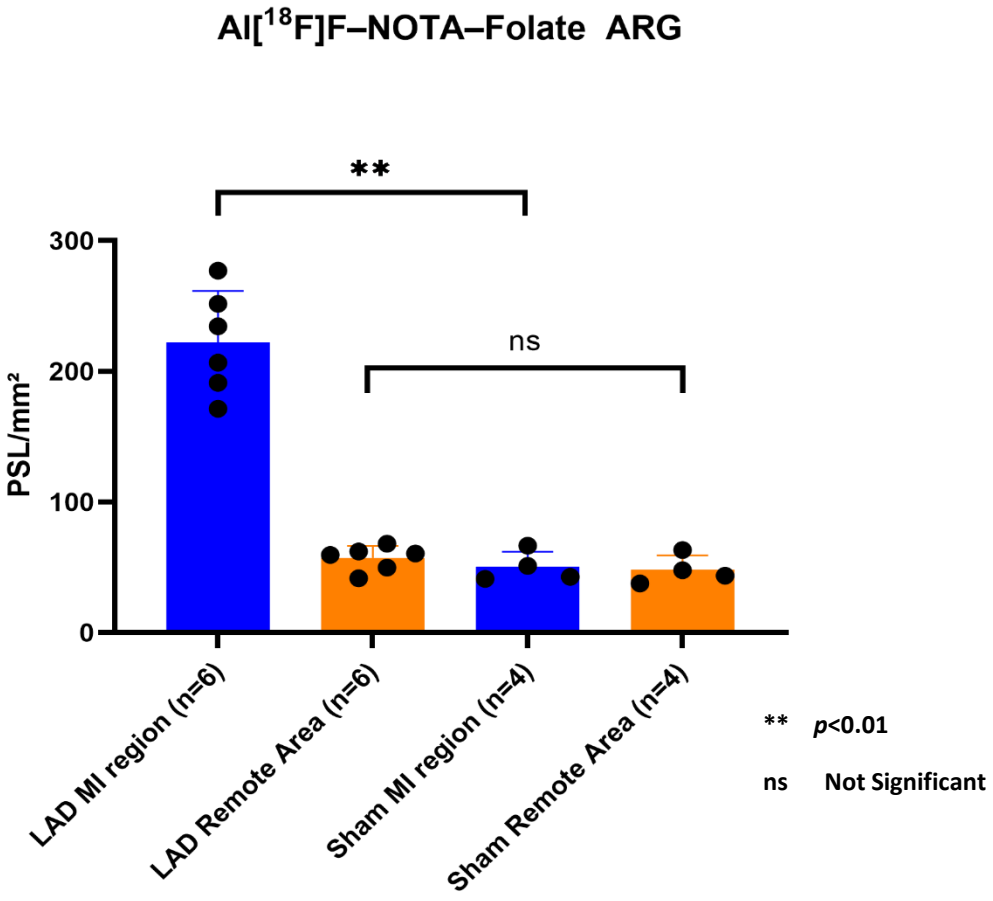

Figure 10. Autoradiography analysis 7 days post-operation

the LAD and sham cohorts exhibited a mean reduction in the uptake of Al[^{18}F]F–NOTA–Folate (88.44 ± 46.52 PSL/mm^2, n = 4 vs. 78.41 ± 13.31 PSL/mm^2, n = 5; *P* = 0.698 (Figure 10).

Digital ARG images of Day 90 post-MI revealed a mean higher uptake of Al[^{18}F]F–NOTA–Folate in the MI regions of LAD group in comparison to the identical site of sham-operated heart sections (205.49 ± 66.21 PSL/mm^2, n = 6 vs. 50.40 ± 10.03 PSL/mm^2, n = 4; *P* = 0.003). In both groups the remote zones showed lower radioactivity.

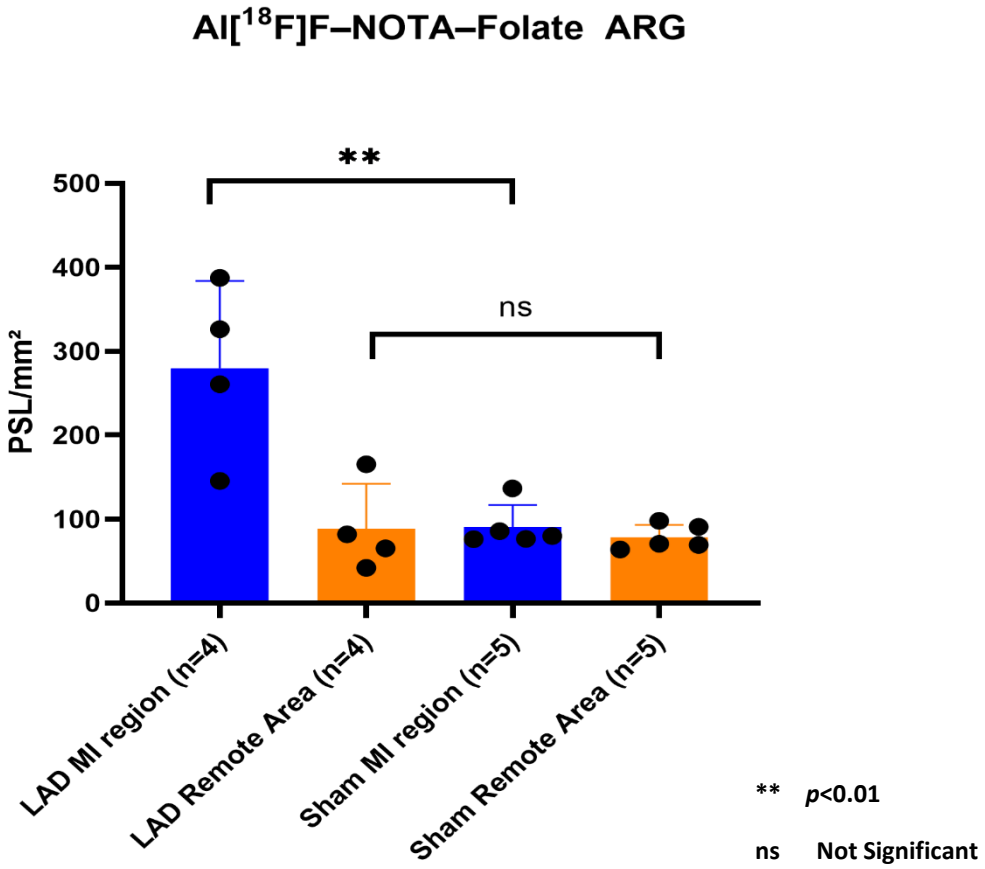

Figure 11. Autoradiography analysis 90 days post-operation

56.99 ± 8.71 PSL/mm^2 in LAD group (n = 6) and 48.04 ± 9.53 PSL/mm^2 in sham group (n = 4) where *P* value was not significant (*P* = 0.208) (Figure 11).

5.3 Image Analysis of CD68 Staining

CD68 stained images were analysed to determine the stained area across the infarcted zone and remote area. The stained area was expressed in percentage (%) in relation to the total infarcted area and a specific part of remote area. The average stained part of a particular area was evaluated by this method. Regarding the sham operated rat, the percentage (%) of stained area was calculated in relation to a part of antero-lateral wall and a part of posterior or medial wall, which determined the infarcted zone and remote area respectively. The stained area provided insight into the macrophage population that had accumulated in that region.

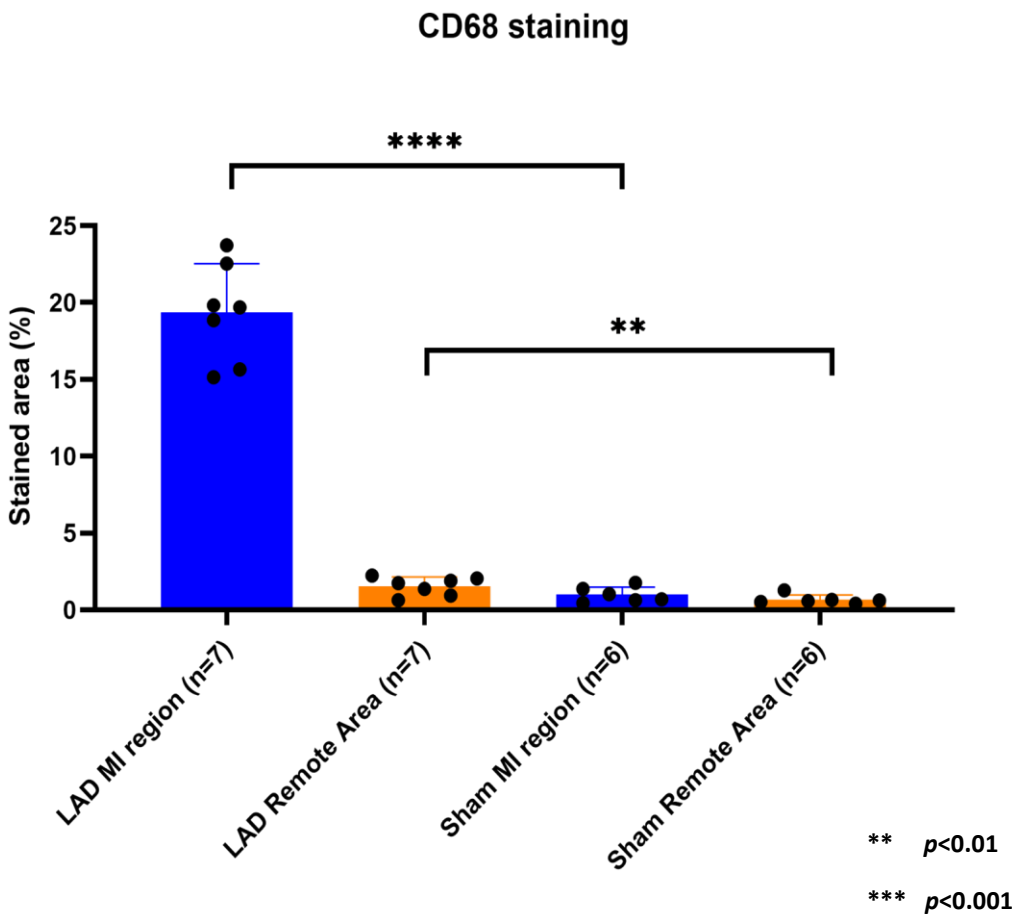

Figure 12. CD68 analysis 3 days after operation

The average area % of CD68 positive staining along the infarcted zones of the LAD group at 3 days post-MI was 19.35 ± 2.96% (n = 7). A mean stained region of 0.99 ± 0.46% (n = 6), with a $P<0.0001$, was seen over the infarcted areas of the sham group. Furthermore, the average stained part was similar across the LAD and sham groups in the remote regions (1.55 ± 0.55%, n = 7 vs. 0.67 ± 0.28%, n = 6; $P = 0.008$) (Figure 12).

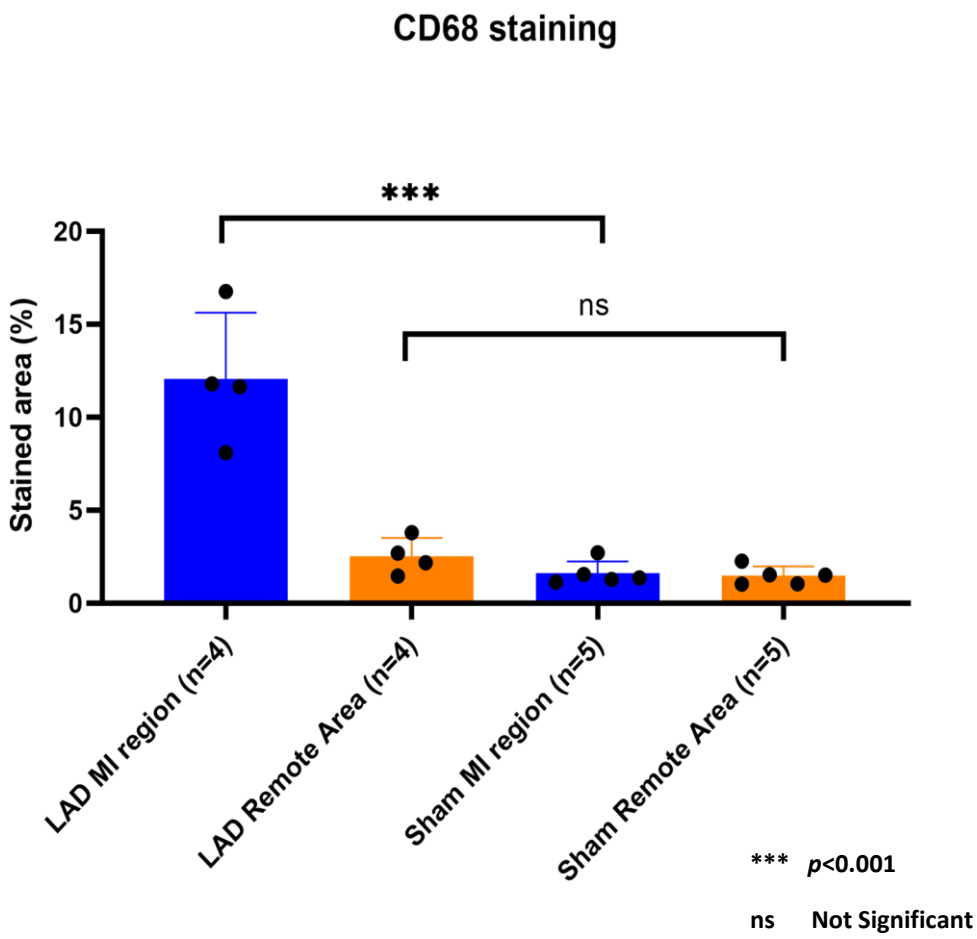

Figure 13. CD68 analysis 7 days post-operation

The area of staining that was detected over the infarcted zones of the LAD group was also assessed 7 days after the MI, and the average value of this expression was determined to be 12.07 ± 3.08% (n = 4). The similar region in the sham group, on the other hand, showed an average stained portion of 1.60 ± 0.57% (n = 5), which resulted in a *P* value that was statistically significant at 0.0003. In addition to this, it was found that the remote areas of

both the LAD and sham groups demonstrated a mean drop in CD68 staining (2.53 ± 0.85%, n = 4 vs. 1.47 ± 0.45%, n = 5; *P* = 0.073) (Figure 13).

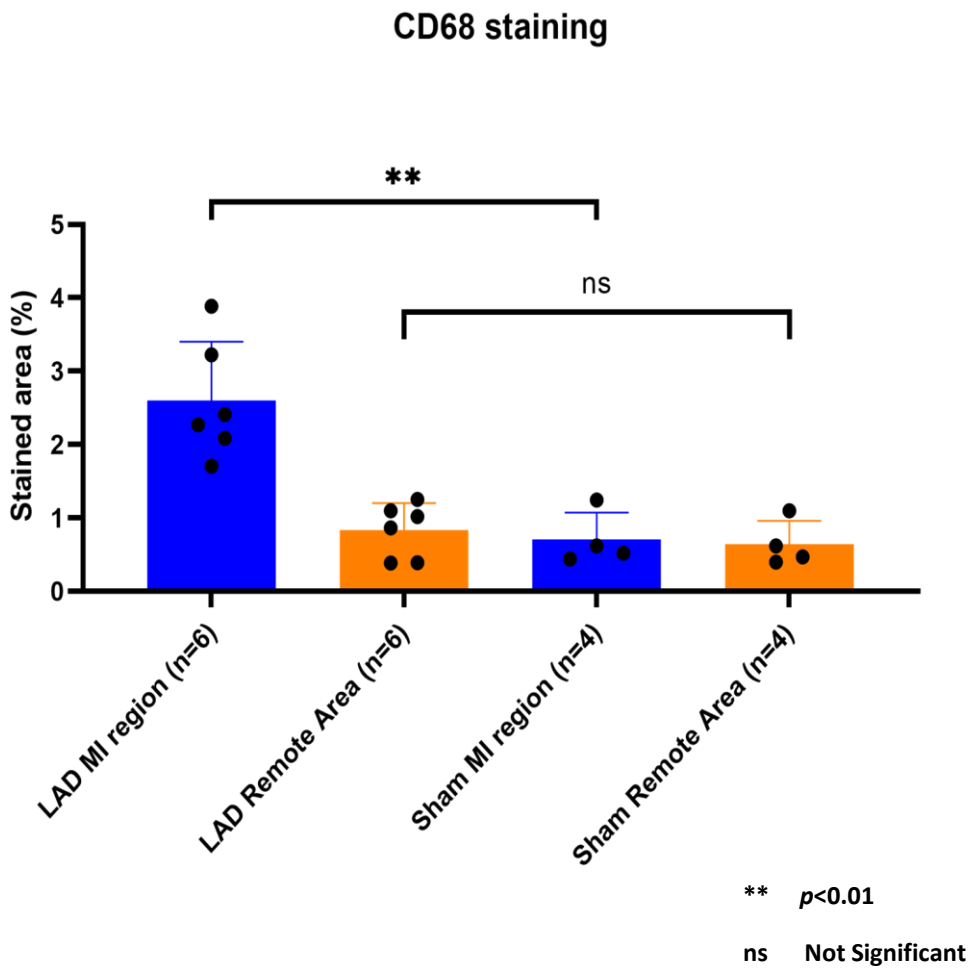

Figure 14. CD68 analysis 90 days after operation

CD68 stained images of Day 90 post-MI indicated a significantly greater mean stained area in the MI regions of the LAD group as compared to the similar location of sham-operated heart sections (2.60 ± 0.74%, n = 6 vs. 0.70 ± 0.32%, n = 4; *P* = 0.003). This was seen in comparison to the MI regions of the sham-operated heart sections. In both groups, the remote zones had a decreased uptake of the stain, with a value of 0.83 ± 0.34% in the LAD group (n = 6) and 0.65 ± 0.27% in the sham group (n = 4), where the *P* value was not statistically significant (*P* = 0.427) (Figure 14).

5.4 Time-course Al[^{18}F]F–NOTA–Folate Uptake

The uptake of Al[^{18}F]F–NOTA–Folate along the MI region at 3 days, 7 days, and 90 days after LAD ligation was compared by using ANOVA test, where it showed *F* value 6.641 and *P* value 0.009. Thus, the uptake of Al[^{18}F]F–NOTA–Folate along the infarcted region over 3 different time points were significantly different and independent. Besides, when Tukey's multiple comparison test was performed between Day 3 post-MI data with Day 90 post-MI data, it was statistically significant (*P* = 0.008). However, when the uptake

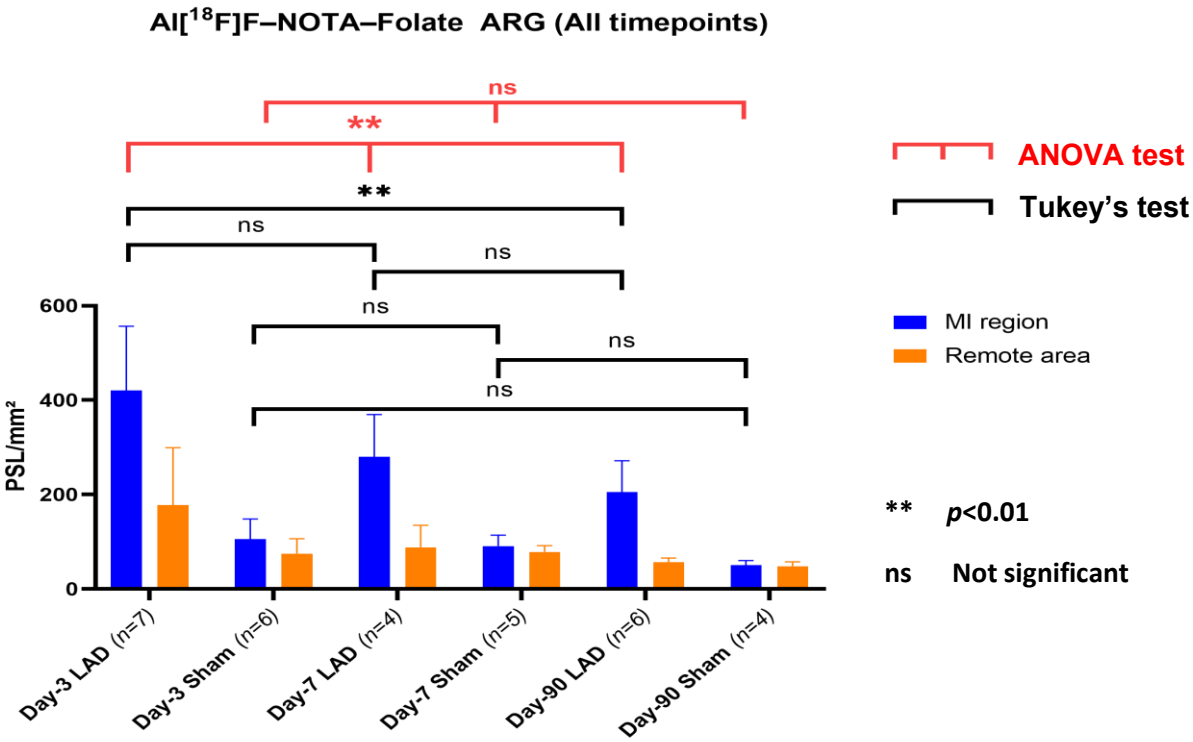

Figure 15. Correlation of Al[^{18}F]F–NOTA–Folate uptake between Day 3, Day 7 and Day 90 time points of all LAD and sham group.

values of Day 3 post-MI were compared with the Day 7 post-MI data ($P = 0.133$), and Day 7 post-MI data with Day 90 post-MI data ($P = 0.570$), both were not significant. The ANOVA test was also performed with the uptake value over the infarcted region of sham-operated rats at the three different time points, but the test was not significant indicating that tracer uptake was similar at all time-points in sham-operated rats. Additionally, the Tukey's multiple comparison test for the sham group at all time points were statistically not significant (Figure 15).

5.5 Time-course CD68 stained image analysis data

The ANOVA test revealed a difference between the infarcted area that was stained 3 days, 7 days, and 90 days after LAD ligation, with a F value of 61.98 and a $P < 0.0001$. The macrophage population along the infarcted area at each of the three times intervals was statistically significantly different. In addition, when comparing the data collected 3 days vs. 7 days after MI ($P = 0.002$); 3 days vs. 90 days after an MI ($P < 0.0001$); and 7 days vs. 90 days after MI ($P = 0.0002$); all the results of these Tukey's multiple comparison tests were statistically significant. The stained area over the infarcted region of sham-operated rats were also analysed using ANOVA at each of the three time-points, although the results were not significant. In case of sham group, Tukey's multiple comparison tests of the stained area at 3 days, 7 days, and 90 days post-operation showed no statistically significant differences (Figure 16).

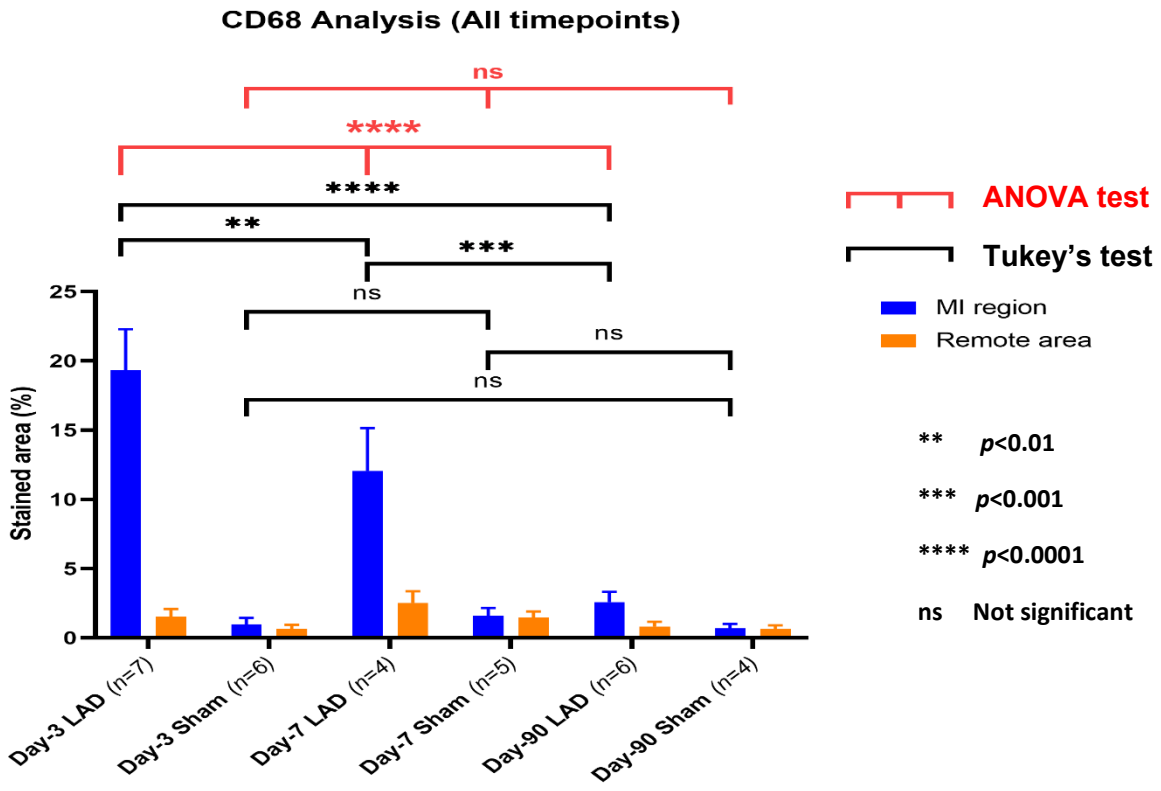

Figure 16. Correlation of CD68 stained (area %) between Day 3, Day 7, and Day 90 time points of all LAD and sham group.

5.6 Correlation Between ARG Analysis and CD68 Staining

The Pearson's correlation test was done among all the infarcted regions of the LAD group (n = 17) at Day 3, Day 7, and Day 90 time points between Al[^{18}F]F–NOTA–Folate uptake in digital ARG and CD68 stained (area %). This showed the *R* value of 0.714, which means it is positively correlated. The *P* value of the test was 0.001 indicating statistically significant difference (Figure 17).

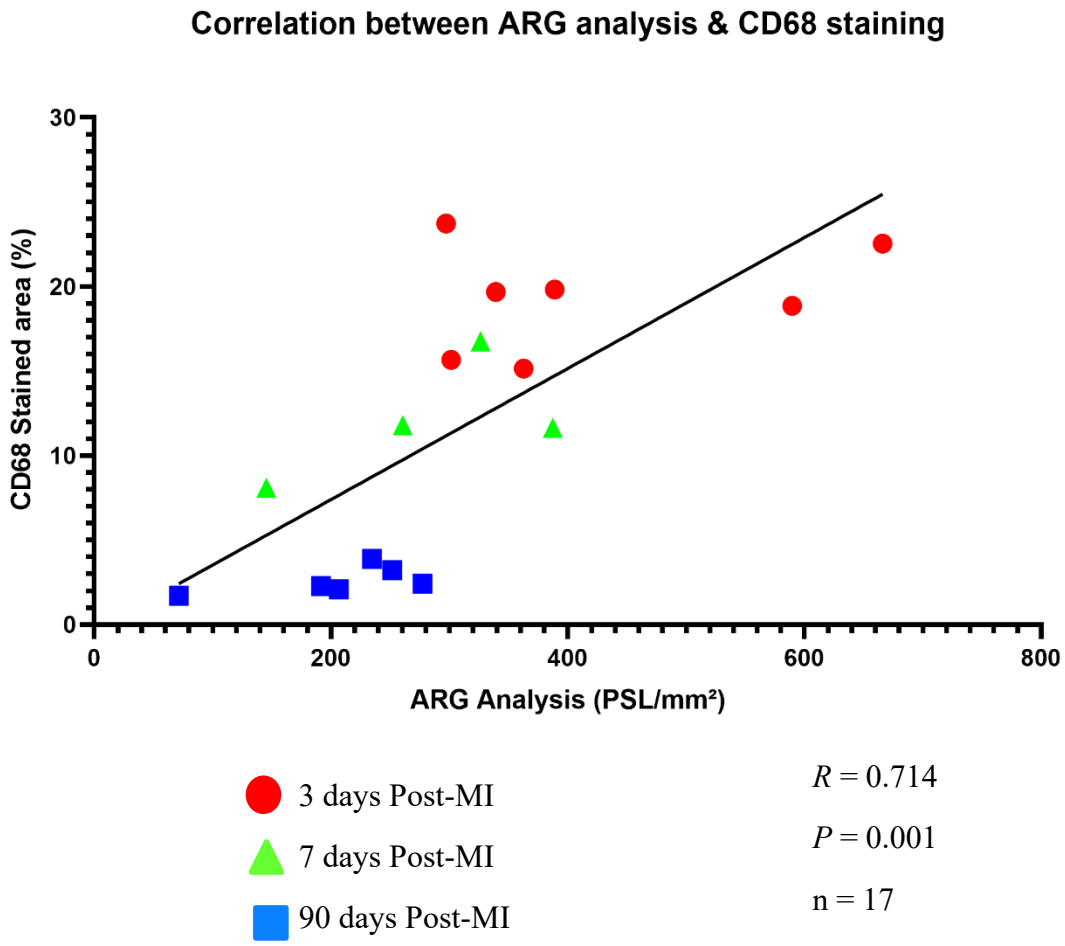

Figure 17. Correlation between Al[^{18}F]F–NOTA–Folate uptake and CD68 staining (area %) in Day 3, Day 7, and Day 90 time points of all LAD groups.

6. DISCUSSION

The overall risk of MI can be strongly impacted by several aspects of individual's lifestyle, including nutritional status, extent of physical activity, smoking habit, intake of alcohol, and ability to manage stress. Making changes to the lifestyle that are beneficial can lower the chance of having a MI and enhance overall heart health. A nutritious diet is essential to preserve healthy heart and lowering the chance of having a MI. Having a diet that is heavy in cholesterol, saturated and trans fats, and salt can raise the chance of having a heart attack. On the other side, consuming a diet that is abundant in fruits, vegetables, whole grains, and lean meats can help lower the chance of having a MI. Participating in regular physical activity is beneficial in the lowering of blood pressure and the reduction of cholesterol levels. Besides, sedentary lifestyle should be avoided along with prohibition of smoking. Cigarette smoking constricts the arteries, which reduces the amount of blood that can flow to the heart and raises the risk of blood clots. Additionally, smoking causes damage to the lining of the arteries, which makes it faster for the plaque to build up and leads to atherosclerosis, a major risk factor of MI. Nicotine also increases the chance of developing lung cancer. Regular intake of significant quantities of alcohol can lead to a rise in blood pressure, contribute to develop atherosclerosis, and raise the risk of arrhythmia and subsequent MI. Despite being aware of all these devastating consequences, the cases of MI in the developed world have been uprising.

Therefore, it is of the utmost importance to make a prompt diagnosis of the condition whenever a patient arrives at the hospital exhibiting the signs and symptoms of MI. In the coming years, patients may be sent for a PET scan shortly after their arrival at the facility. In order to provide an easy evaluation of MI, such as the visualisation of the extent of tissue damage, *in vivo* PET scan is a possible imaging modality. It is necessary to have a complete understanding of the infarcted or necrotic region to plan the subsequent treatment protocol and anticipate the prognosis. However, it is not practical to conduct experiments using radiotracers directly on human bodies due to the risk of being exposed to the radiation and experiencing the unanticipated side effects. Because of these factors,

it is very necessary to conduct the pre-clinical testing of newly synthesised radiotracers for the purpose of detecting a particular disease and to assess the effectiveness as well.

MI and other cardiovascular diseases are frequently studied using the rat LAD MI model. Despite its widespread use and beneficial insights into the pathophysiology of MI, this model has some possible drawbacks. The operation was quite complicated. LAD artery is always difficult to identify clearly and ligate perfectly. It was important to pick the right animal for the experiment. The mortality rate of the surgery was approximately 50%, so more animals were needed to perform the surgery, which was time-consuming also. In addition, there was a probability that the experimental outcomes might be affected by the use of anaesthesia and analgesics.

There were many technical difficulties found in the rat LAD MI model, and the infarct size can vary widely between animals. Because of this, comparing data from multiple experiments and drawing firm conclusions can be challenging. These drawbacks were minimized through image analysis steps. The uptake of Al[^{18}F]F–NOTA–Folate ARG was calculated in PSL/mm^2 and CD68 staining was measured in %. So it was easy to compare between them in spite of having different infarcted region.

The capabilities of the ARG image analysis software TINA were constrained. The ROIs drawn directly on the H & E images could not be superimposed over ARG images by using this software. Because of this another software GIMP was used to perform these steps. It also required a significant amount of time and increased the complicacy in the image analysis step. The defined regions of interest and the analytic configuration in TINA is user oriented. This may compromise the repeatability of the analysis by introducing subjectivity and variation into the findings.

At Day 3 post-operation, when we compared the data of both Al[^{18}F]F–NOTA–Folate ARG and CD68 staining, LAD MI region vs. the same area in sham-operated and LAD remote area vs. sham remote area, all were significantly correlated. The Al[^{18}F]F–NOTA–Folate ARG uptake of LAD MI region was more than double compared to the same area in sham-operated. Although the CD68 stained (%) area of the infarcted region of LAD group was almost 10 times higher than all other defined region. The sham group or the remote area were not expected to correlate statistically. However, this was the only time point that all data had significant correlation.

On postoperative Day 7, a substantial correlation was found between the LAD MI region and the corresponding sham-operated region using data from both Al[^{18}F]F-NOTA-Folate ARG and CD68 staining. Uptake of Al[^{18}F]F-NOTA-Folate ARG was three times greater in the LAD MI region than in the same region of sham model. Despite this, the percentage of LAD group infarcted area that was CD68 stained was nearly four times higher than that of any other specified region. There was no anticipation of any statistical connections between the sham group or the remote area. At this point in time, the only statistically significant association was established between the LAD MI region and the same sham-operated area.

On Day 90 post-operation, utilising data from both Al[^{18}F]F-NOTA-Folate ARG uptake and CD68 staining (area %), there was a strong correlation was established between the LAD MI region and the equivalent sham-operated region. In the LAD MI area, uptake of the Al[^{18}F]F-NOTA-Folate ARG was four times higher than the same area of sham model. Despite this, the percentage of CD68 staining along the infarcted region of the LAD MI group was roughly three times higher than that of any other specified area. The data revealed in the LAD remote area, the same area of sham-operated one, and the sham remote area were very identical. There was no expectation that the sham group or the remote area would share any statistical links with one another. At this point in time, the only link that had been shown to be statistically significant is the one that had been formed between the LAD MI region and the same area of sham model.

When the graph of Al[^{18}F]F-NOTA-Folate ARG uptake at all time points was observed, it was visible that there was a decreasing trend from Day 3 uptake value to the Day 90 value. As the ANOVA test was significant only in the LAD MI region of 3 time points, it was indicated that the data were normally distributed and had independent value. The null hypothesis was rejected. The Tukey's multiple correlation test was not significant during the comparison between Day 3 vs. Day 7 and Day 7 vs. Day 90 LAD MI region. There was a probability to relate them if we could gather more data at those time points. The sham MI region had a variable uptake value, because of that it was not expected to correlate statistically.

It was clear from viewing the graph of CD68 stained (%) area over time that the value dropped steadily from Day 3 to Day 90. Results from ANOVA test showed that the data had a normal distribution and exhibited independent value solely in the LAD MI region across all the three time periods. When comparing the LAD MI region on Day 3, Day 7, and Day 90, the Tukey's multiple correlation test found significant in all time points. The stained area of sham-operated sections as equivalent as LAD MI region has no consistency, so that the correlation could not be predicted.

The Pearson's correlation was significant all together in only LAD MI region. There was lack of correlation at individual timepoints, because of the number of animals. The standard deviation higher in remote areas compared the infarcted region. Besides, the sham group has also variable values, therefore it was not expected that these regions had positive correlation. The macrophage populated area in CD68 images had higher uptake value of Al[^{18}F]F-NOTA-Folate in ARG images.

7. CONCLUSION

Inflammation after MI can be visualized with FR-β-targeted Al[^{18}F]F–NOTA–Folate PET tracer targeting activated macrophages. In the MI model, infarcted cardiac areas had higher tracer uptake in *ex vivo* autoradiography compared to the remote areas or corresponding regions in the sham-operated rats. Furthermore, anti-CD68 immunohistochemical staining demonstrated increased macrophage activity in the infarcted areas. The Al[^{18}F]F–NOTA–Folate uptake in the infarcted area and amount of CD68-positive cells correlated positively and significantly. Imaging of FR-β expressed on activated macrophages with the novel Al[^{18}F]F–NOTA–Folate PET tracer is a promising tool for non-invasive imaging of inflammation in MI.

Activated macrophages are found abundantly in any type of inflammation, with expression of FR-β. Many studies have been done previously to target this receptor in other disease models, most of the studies are found promising. This is the first time we have used the Al[^{18}F]F–NOTA–Folate radiotracer to target FR-β receptor in the MI disease model.

.

8. ACKNOWLEDGEMENTS

I am grateful to my supervisors Professor Anne Roivainen and Professor Antti Saraste, from the bottom of my heart for letting me participate in research in their wonderful lab, and their enormous support, and guidance. My sincerest of gratitude to Imran Iqbal for his advice and guidance throughout my thesis project, specifically mentoring all the laboratory procedures and image analysis methods.

I would also like to give thanks to my colleagues in the group Heidi Liljenbäck, Aake Petteri Honkaniemi, Jenni Virta, Putri Andriana, Erika Atencio Herre, and Maxwell Miner for their invaluable support provided during the experiments. Additionally, thanks to Erica Nyman and Marja-Riitta Kajaala (Histocore, Institute of Biomedicine, University of Turku) for tissue sectioning and staining.

Thanks to Turku PET Centre to provide me all logistical support and awarding me the Master's Thesis Grant.

My appreciation towards BIMA family especially Professor Diana Toiovola who provided guidance and assistance during the completion of my study. Moreover, this work would have been unattainable without the training I received from Achol Bhowmik.

While it is impossible to adequately express my gratitude, I would like to express my deepest appreciation to my continuous support specifically my father Abu Hossain Talukder, my wife Tamanna Siddiqa, my daughter Amyra Turaya, my mother-in-law Tahmina Begum and my brother-in-law Arifur Rahman and Akbar Hossain. Thank you for your valuable support.

I would like to dedicate this thesis to my mother, **Anowara Begum**, whose encouragement led me to pursue this graduation study. Her inspiration and motivation provided me with the fortitude to persevere through seemingly insurmountable obstacles.

In loving memory of my mother **Anowara Begum**

(January 1,1954 to May 7, 2008)

9. REFERENCES

Alexander, J. H., & Smith, P. K. (2016). Coronary-Artery Bypass Grafting. *New England Journal of Medicine*, *374*(20), 1954–1964. https://doi.org/10.1056/NEJMra1406944

Anderson, J. L., & Morrow, D. A. (2017). Acute Myocardial Infarction. *New England Journal of Medicine*, *376*(21), 2053–2064. https://doi.org/10.1056/NEJMra1606915

Bäck, T., & Jacobsson, L. (2010). The α-Camera: A Quantitative Digital Autoradiography Technique Using a Charge-Coupled Device for Ex Vivo High-Resolution Bioimaging of α-Particles. *Journal of Nuclear Medicine*, *51*(10), 1616–1623. https://doi.org/10.2967/jnumed.110.077578

Bailey, D. L. (Ed.). (2005). *Positron emission tomography: Basic sciences*. Springer.

Barthe, N., Maîtrejean, S., Carvou, N., & Cardona, A. (2020). High-resolution beta imaging. In *Handbook of Radioactivity Analysis: Volume 2* (pp. 669–727). Elsevier. https://doi.org/10.1016/B978-0-12-814395-7.00009-X

Brenner, D. J. (2007). Computed Tomography—An Increasing Source of Radiation Exposure. *The New England Journal of Medicine*.

Bularga, A., Hung, J., Daghem, M., Stewart, S., Taggart, C., Wereski, R., Singh, T., Meah, M. N., Fujisawa, T., Ferry, A. V., Chiong, J., Jenkins, W. S., Strachan, F. E., Semple, S., van Beek, E. J. R., Williams, M., Dey, D., Tuck, C., Baker, A. H., … Chapman, A. R. (2022). Coronary Artery and Cardiac Disease in Patients With Type 2 Myocardial Infarction: A Prospective Cohort Study. *Circulation*, *145*(16), 1188–1200. https://doi.org/10.1161/CIRCULATIONAHA.121.058542

Burke, A. P., & Virmani, R. (2007). Pathophysiology of Acute Myocardial Infarction. *Medical Clinics of North America*, *91*(4), 553–572. https://doi.org/10.1016/j.mcna.2007.03.005

Cantatore, A., & Müller, P. (n.d.). *Introduction to computed tomography*.

Chan, D., & Ng, L. L. (2010). *RBeivoiewmarkers in acute myocardial infarction*. 11.

Chen, Q., Meng, X., McQuade, P., Rubins, D., Lin, S.-A., Zeng, Z., Haley, H., Miller, P., González Trotter, D., & Low, P. S. (2016). Synthesis and Preclinical Evaluation of Folate-NOTA-Al ^{18} F for PET Imaging of Folate-Receptor-Positive Tumors. *Molecular Pharmaceutics*, *13*(5), 1520–1527. https://doi.org/10.1021/acs.molpharmaceut.5b00989

Cheng, Y., & Rong, J. (2018). Macrophage Polarization as a Therapeutic Target in Myocardial Infarction. *Current Drug Targets*, *19*(6), 651–662. https://doi.org/10.2174/1389450118666171031115025

Christia, P., & Frangogiannis, N. G. (2013). Targeting inflammatory pathways in myocardial infarction. *European Journal of Clinical Investigation*, *43*(9), 986–995. https://doi.org/10.1111/eci.12118

De Matos, L. L., Trufelli, D. C., De Matos, M. G. L., & Da Silva Pinhal, M. A. (2010). Immunohistochemistry as an Important Tool in Biomarkers Detection and Clinical Practice. *Biomarker Insights*, *5*, BMI.S2185. https://doi.org/10.4137/BMI.S2185

DeFilippis, A. P., Lidani, K. C. F., Nam, Y., Trainor, P. J., Johnson, W. C., Heckbert, S. R., McClelland, R. L., Blaha, M. J., & Nasir, K. (2023). Risk factor associations with individual myocardial infarction subtypes and acute non-ischemic myocardial injury in the Multi-Ethnic Study of Atherosclerosis (MESA): Design and rationale. *American Heart Journal*, S0002870323000479. https://doi.org/10.1016/j.ahj.2023.02.012

Ducas, R. A., Labos, C., Allen, D., Golian, M., Jeyaraman, M., Lys, J., Mann, A., Copstein, L., Vokey, S., Rabbani, R., Zarychanski, R., Abou-Setta, A. M., & Menkis, A. H. (2016). Association of Pre-hospital ECG Administration With Clinical Outcomes in ST-Segment Myocardial Infarction: A Systematic Review and Meta-analysis. *Canadian Journal of Cardiology*, *32*(12), 1531–1541. https://doi.org/10.1016/j.cjca.2016.06.004

Elnakat, H. (2004). Distribution, functionality and gene regulation of folate receptor isoforms: Implications in targeted therapy. *Advanced Drug Delivery Reviews*, *56*(8), 1067–1084. https://doi.org/10.1016/j.addr.2004.01.001

Esmaeilzadeh, M., & Parsaee, M. (2013). *The Role of Echocardiography in Coronary Artery Disease and Acute Myocardial Infarction*.

Fadok, V. A., Bratton, D. L., Konowal, A., Freed, P. W., Westcott, J. Y., & Henson, P. M. (1998). Macrophages that have ingested apoptotic cells in vitro inhibit proinflammatory cytokine production through autocrine/paracrine mechanisms

involving TGF-beta, PGE2, and PAF. *Journal of Clinical Investigation*, *101*(4), 890–898. https://doi.org/10.1172/JCI1112

Fanchon, L. M., Dogan, S., Moreira, A. L., Carlin, S. A., Schmidtlein, C. R., Yorke, E., Apte, A. P., Burger, I. A., Durack, J. C., Erinjeri, J. P., Maybody, M., Schöder, H., Siegelbaum, R. H., Sofocleous, C. T., Deasy, J. O., Solomon, S. B., Humm, J. L., & Kirov, A. S. (2015). Feasibility of In Situ, High-Resolution Correlation of Tracer Uptake with Histopathology by Quantitative Autoradiography of Biopsy Specimens Obtained Under ^{18} F-FDG PET/CT Guidance. *Journal of Nuclear Medicine*, *56*(4), 538–544. https://doi.org/10.2967/jnumed.114.148668

Fichet, P., Bresson, F., Leskinen, A., Goutelard, F., Ikonen, J., & Siitari-Kauppi, M. (2012). Tritium analysis in building dismantling process using digital autoradiography. *Journal of Radioanalytical and Nuclear Chemistry*, *291*(3), 869–875. https://doi.org/10.1007/s10967-011-1423-1

Fleischmann, D., & Boas, F. E. (2011). Computed tomography—Old ideas and new technology. *European Radiology*, *21*(3), 510–517. https://doi.org/10.1007/s00330-011-2056-z

Frantz, S., Hundertmark, M. J., Schulz-Menger, J., Bengel, F. M., & Bauersachs, J. (2022). Left ventricular remodelling post-myocardial infarction: Pathophysiology, imaging, and novel therapies. *European Heart Journal*, *43*(27), 2549–2561. https://doi.org/10.1093/eurheartj/ehac223

Garvey, C. J. (2002). Computed tomography in clinical practice. *BMJ*, *324*(7345), 1077–1080. https://doi.org/10.1136/bmj.324.7345.1077

Grech, E. D. (2003). Percutaneous coronary intervention. I: History and development. *BMJ*, *326*(7398), 1080–1082. https://doi.org/10.1136/bmj.326.7398.1080

Green, G. E., Stertzer, S. H., & Reppert, E. H. (1968). Coronary Arterial Bypass Grafts. *The Annals of Thoracic Surgery*, *5*(5), 443–450. https://doi.org/10.1016/S0003-4975(10)66377-1

Hampel, U. (2022). X-ray computed tomography. In *Industrial Tomography* (pp. 207–229). Elsevier. https://doi.org/10.1016/B978-0-12-823015-2.00029-7

Hegi-Johnson, F., Rudd, S., Hicks, R. J., De Ruysscher, D., Trapani, J. A., John, T., Donnelly, P., Blyth, B., Hanna, G., Everitt, S., Roselt, P., & MacManus, M. P. (2022).

Imaging immunity in patients with cancer using positron emission tomography. *Npj Precision Oncology*, *6*(1), 24. https://doi.org/10.1038/s41698-022-00263-x

Hoffmann, U., Bamberg, F., Chae, C. U., Nichols, J. H., Rogers, I. S., Seneviratne, S. K., Truong, Q. A., Cury, R. C., Abbara, S., Shapiro, M. D., Moloo, J., Butler, J., Ferencik, M., Lee, H., Jang, I.-K., Parry, B. A., Brown, D. F., Udelson, J. E., Achenbach, S., … Nagurney, J. T. (2009). Coronary Computed Tomography Angiography for Early Triage of Patients With Acute Chest Pain. *Journal of the American College of Cardiology*, *53*(18), 1642–1650. https://doi.org/10.1016/j.jacc.2009.01.052

Horowitz, R. S., Morganroth, J., Parrotto, C., Chen, C. C., Soffer, J., & Pauletto, F. J. (1982). Immediate diagnosis of acute myocardial infarction by two-dimensional echocardiography. *Circulation*, *65*(2), 323–329. https://doi.org/10.1161/01.CIR.65.2.323

Jager, N. A., Westra, J., Golestani, R., van Dam, G. M., Low, P. S., Tio, R. A., Slart, R. H. J. A., Boersma, H. H., Bijl, M., & Zeebregts, C. J. (2014). Folate Receptor-β Imaging Using ^{99m} Tc-Folate to Explore Distribution of Polarized Macrophage Populations in Human Atherosclerotic Plaque. *Journal of Nuclear Medicine*, *55*(12), 1945–1951. https://doi.org/10.2967/jnumed.114.143180

Jiang, Chalich, & Deen. (2019). Sensors for Positron Emission Tomography Applications. *Sensors*, *19*(22), 5019. https://doi.org/10.3390/s19225019

Jin, C., Luo, X., Li, X., Zhou, R., Zhong, Y., Xu, Z., Cui, C., Xing, X., Zhang, H., & Tian, M. (2022). Positron emission tomography molecular imaging-based cancer phenotyping. *Cancer*, *128*(14), 2704–2716. https://doi.org/10.1002/cncr.34228

Johnston, R. F., Pickett, S. C., & Barker, D. L. (1990). Autoradiography using storage phosphor technology. *Electrophoresis*, *11*(5), 355–360. https://doi.org/10.1002/elps.1150110503

Kalender, W. A. (2006). X-ray computed tomography. *Physics in Medicine and Biology*, *51*(13), R29–R43. https://doi.org/10.1088/0031-9155/51/13/R03

Kazi, S. N., Von Huben, A., Marschner, S., Chong, J. J. H., Denniss, A. R., Ong, A. T. L., & Chow, C. K. (2023). Trends in Modifiable Risk Factors Amongst First Presentation ST Elevation Myocardial Infarction Patients in a Large Longitudinal

Registry. *Heart, Lung and Circulation*, S1443950623000227. https://doi.org/10.1016/j.hlc.2022.12.012

Kelemen, L. E. (2006). The role of folate receptor α in cancer development, progression and treatment: Cause, consequence or innocent bystander? *International Journal of Cancer*, *119*(2), 243–250. https://doi.org/10.1002/ijc.21712

Kim, E. E., Lee, M.-C., Inoue, T., & Wong, W.-H. (Eds.). (2013). *Clinical PET and PET/CT: Principles and Applications*. Springer New York. https://doi.org/10.1007/978-1-4419-0802-5

Koene, R. J., Prizment, A. E., Blaes, A., & Konety, S. H. (2016). Shared Risk Factors in Cardiovascular Disease and Cancer. *Circulation*, *133*(11), 1104–1114. https://doi.org/10.1161/CIRCULATIONAHA.115.020406

Koivunen, M., Tynkkynen, J., Oksala, N., Eskola, M., & Hernesniemi, J. (2023). Incidence of sudden cardiac arrest and sudden cardiac death after unstable angina pectoris and myocardial infarction. *American Heart Journal*, *257*, 9–19. https://doi.org/10.1016/j.ahj.2022.11.009

Kunadian, V., & Gibson, C. M. (2012). Thrombolytics and Myocardial Infarction: Thrombolytics and Myocardial Infarction. *Cardiovascular Therapeutics*, *30*(2), e81–e88. https://doi.org/10.1111/j.1755-5922.2010.00239.x

Lambert, J. M., Lopez, E. F., & Lindsey, M. L. (2008). Macrophage roles following myocardial infarction. *International Journal of Cardiology*, *130*(2), 147–158. https://doi.org/10.1016/j.ijcard.2008.04.059

Lameka, K., Farwell, M. D., & Ichise, M. (2016). Positron Emission Tomography. In *Handbook of Clinical Neurology* (Vol. 135, pp. 209–227). Elsevier. https://doi.org/10.1016/B978-0-444-53485-9.00011-8

Leancă, S. A., Crișu, D., Petriș, A. O., Afrăsânie, I., Genes, A., Costache, A. D., Tesloianu, D. N., & Costache, I. I. (2022). Left Ventricular Remodeling after Myocardial Infarction: From Physiopathology to Treatment. *Life*, *12*(8), 1111. https://doi.org/10.3390/life12081111

Lear, J. L., Plotnick, J., & Rumley, S. (n.d.). *Development, and Evaluation of a Solid-State Image Analyzer*.

Mannaerts, H. (2004). Early identification of left ventricular remodelling after myocardial infarction, assessed by transthoracic 3D echocardiography. *European Heart Journal*, *25*(8), 680–687. https://doi.org/10.1016/j.ehj.2004.02.030

Martinez, F. O., & Gordon, S. (2014). The M1 and M2 paradigm of macrophage activation: Time for reassessment. *F1000Prime Reports*, *6*. https://doi.org/10.12703/P6-13

Melly, L., Torregrossa, G., Lee, T., Jansens, J.-L., & Puskas, J. D. (2018). Fifty years of coronary artery bypass grafting. *Journal of Thoracic Disease*, *10*(3), 1960–1967. https://doi.org/10.21037/jtd.2018.02.43

Mouton, A. J., DeLeon-Pennell, K. Y., Rivera Gonzalez, O. J., Flynn, E. R., Freeman, T. C., Saucerman, J. J., Garrett, M. R., Ma, Y., Harmancey, R., & Lindsey, M. L. (2018). Mapping macrophage polarization over the myocardial infarction time continuum. *Basic Research in Cardiology*, *113*(4), 26. https://doi.org/10.1007/s00395-018-0686-x

Muehllehner, G., & Karp, J. S. (2006). Positron emission tomography. *Physics in Medicine and Biology*, *51*(13), R117–R137. https://doi.org/10.1088/0031-9155/51/13/R08

Nieman, K., Cury, R. C., Ferencik, M., Nomura, C. H., Abbara, S., Hoffmann, U., Gold, H. K., Jang, I.-K., & Brady, T. J. (2006). Differentiation of Recent and Chronic Myocardial Infarction by Cardiac Computed Tomography. *The American Journal of Cardiology*, *98*(3), 303–308. https://doi.org/10.1016/j.amjcard.2006.01.101

Nikolaou, K., Knez, A., Sagmeister, S., Wintersperger, B. J., Boekstegers, P., Steinbeck, G., Reiser, M. F., & Becker, C. R. (2004). Assessment of Myocardial Infarctions Using Multidetector-Row Computed Tomography: *Journal of Computer Assisted Tomography*, *28*(2), 286–292. https://doi.org/10.1097/00004728-200403000-00021

Ollinger, J. M., & Fessler, J. A. (1997). Positron-emission tomography. *IEEE Signal Processing Magazine*, *14*(1), 43–55. https://doi.org/10.1109/79.560323

Panju, A. A. (1998). Is This Patient Having a Myocardial Infarction? *JAMA*, *280*(14), 1256. https://doi.org/10.1001/jama.280.14.1256

Piña, R., Santos-Díaz, A. I., Orta-Salazar, E., Aguilar-Vazquez, A. R., Mantellero, C. A., Acosta-Galeana, I., Estrada-Mondragon, A., Prior-Gonzalez, M., Martinez-Cruz, J. I., & Rosas-Arellano, A. (2022). Ten Approaches That Improve Immunostaining: A Review of the Latest Advances for the Optimization of Immunofluorescence. *International Journal of Molecular Sciences*, *23*(3), 1426. https://doi.org/10.3390/ijms23031426

Pina-Cabral, L. B., Carvalhais, V., Mesquita, B., Escórcio, C., Silva, P. F., Pinto, P., Napoleão, P., Pinheiro, T., Monteiro, M. C., Almeida-Dias, A., & Criado, B. (2018). Myocardial infarction before and after the age of 45: Possible role of platelet receptor polymorphisms. *Revista Portuguesa de Cardiologia (English Edition)*, *37*(9), 727–735. https://doi.org/10.1016/j.repce.2018.03.017

Rafieian-Kopaei, M., Setorki, M., Doudi, M., Baradaran, A., & Nasri, H. (2014). Atherosclerosis: Process, Indicators, Risk Factors and New Hopes. *International Journal of Preventive Medicine*, *5*(8), 20.

Raichle, M. E. (n.d.). Positron Emission Tomography. *POSITRON EMISSION TOMOGRAPHY*, 19.

Reed, G. W., Rossi, J. E., & Cannon, C. P. (2017). Acute myocardial infarction. *The Lancet*, *389*(10065), 197–210. https://doi.org/10.1016/S0140-6736(16)30677-8

Ribichini, F., Pugno, F., Ferrero, V., Bussolati, G., Feola, M., Russo, P., Di Mario, C., Colombo, A., & Vassanelli, C. (2006). Cellular Immunostaining of Angiotensin-Converting Enzyme in Human Coronary Atherosclerotic Plaques. *Journal of the American College of Cardiology*, *47*(6), 1143–1149. https://doi.org/10.1016/j.jacc.2005.12.022

Richter, T., Nahrig, J., Komminoth, P., Kowolik, J., & Werner, M. (1999). Protocol for ultrarapid immunostaining of frozen sections. *Journal of Clinical Pathology*, *52*(6), 461–463. https://doi.org/10.1136/jcp.52.6.461

Roger, V. L. (2007). Epidemiology of Myocardial Infarction. *Medical Clinics of North America*, *91*(4), 537–552. https://doi.org/10.1016/j.mcna.2007.03.007

Ross, J. F., Chaudhuri, P. K., & Ratnam, M. (1994). Differential regulation of folate receptor isoforms in normal and malignant tissues in vivo and in established cell lines. Physiologic and clinical implications. *Cancer*, *73*(9), 2432–2443.

https://doi.org/10.1002/1097-0142(19940501)73:9<2432::AID-CNCR2820730929>3.0.CO;2-S

Sagris, M., Antonopoulos, A. S., Theofilis, P., Oikonomou, E., Siasos, G., Tsalamandris, S., Antoniades, C., Brilakis, E. S., Kaski, J. C., & Tousoulis, D. (2022). Risk factors profile of young and older patients with myocardial infarction. *Cardiovascular Research*, *118*(10), 2281–2292. https://doi.org/10.1093/cvr/cvab264

Saleh, M., & Ambrose, J. A. (2018). Understanding myocardial infarction. *F1000Research*, *7*, 1378. https://doi.org/10.12688/f1000research.15096.1

Santoro, G. M., Valenti, R., Buonamici, P., Bolognese, L., Cerisano, G., Moschi, G., Trapani, M., Antoniucci, D., & Fazzini, P. F. (1998). Relation between ST-segment changes and myocardial perfusion evaluated by myocardial contrast echocardiography in patients with acute myocardial infarction treated with direct angioplasty. *The American Journal of Cardiology*, *82*(8), 932–937. https://doi.org/10.1016/S0002-9149(98)00508-6

Schmitt, C., Lehmann, G., Schmieder, S., Karch, M., Neumann, F.-J., & Scho¨mig, A. (2001). Diagnosis of Acute Myocardial Infarction in Angiographically Documented Occluded Infarct Vessel. *Chest*, *120*(5), 1540–1546. https://doi.org/10.1378/chest.120.5.1540

Serruys, P. W., Morice, M.-C., Kappetein, A. P., Colombo, A., Holmes, D. R., Mack, M. J., Ståhle, E., Feldman, T. E., van den Brand, M., Bass, E. J., Van Dyck, N., Leadley, K., Dawkins, K. D., & Mohr, F. W. (2009). Percutaneous Coronary Intervention versus Coronary-Artery Bypass Grafting for Severe Coronary Artery Disease. *New England Journal of Medicine*, *360*(10), 961–972. https://doi.org/10.1056/NEJMoa0804626

Sgarbossa, E. B., Underwood, D. A., & Wagner, G. S. (1996). Electrocardiographic Diagnosis of Evolving Acute Myocardial Infarction in the Presence of Left Bundle-Branch Block. *The New England Journal of Medicine*, *334*(8).

Shiraishi, M., Shintani, Y., Shintani, Y., Ishida, H., Saba, R., Yamaguchi, A., Adachi, H., Yashiro, K., & Suzuki, K. (2016). Alternatively activated macrophages determine repair of the infarcted adult murine heart. *Journal of Clinical Investigation*, *126*(6), 2151–2166. https://doi.org/10.1172/JCI85782

Smit, M., Coetzee, A. R., & Lochner, A. (2020). The Pathophysiology of Myocardial Ischemia and Perioperative Myocardial Infarction. *Journal of Cardiothoracic and Vascular Anesthesia*, *34*(9), 2501–2512. https://doi.org/10.1053/j.jvca.2019.10.005

Smith-Bindman, R. (2010). Is Computed Tomography Safe? *New England Journal of Medicine*, *363*(1), 1–4. https://doi.org/10.1056/NEJMp1002530

Steinz, M. M., Ezdoglian, A., Khodadust, F., Molthoff, C. F. M., Srinivasarao, M., Low, P. S., Zwezerijnen, G. J. C., Yaqub, M., Beaino, W., Windhorst, A. D., Tas, S. W., Jansen, G., & van der Laken, C. J. (2022). Folate Receptor Beta for Macrophage Imaging in Rheumatoid Arthritis. *Frontiers in Immunology*, *13*, 819163. https://doi.org/10.3389/fimmu.2022.819163

Suthipintawong, C., Leong, A. S.-Y., & Vinyuvat, S. (1996). Immunostaining of cell preparations: A comparative evaluation of common fixatives and protocols. *Diagnostic Cytopathology*, *15*(2), 167–174. https://doi.org/10.1002/(SICI)1097-0339(199608)15:2<167::AID-DC17>3.0.CO;2-F

The SCOT-HEART Investigators. (2018). Coronary CT Angiography and 5-Year Risk of Myocardial Infarction. *New England Journal of Medicine*, *379*(10), 924–933. https://doi.org/10.1056/NEJMoa1805971

Thygesen, K., Alpert, J. S., Jaffe, A. S., Chaitman, B. R., Bax, J. J., Morrow, D. A., & White, H. D. (2018). Fourth Universal Definition of Myocardial Infarction (2018). *Journal of the American College of Cardiology*, *72*(18), 2231–2264. https://doi.org/10.1016/j.jacc.2018.08.1038

Timmis, A., Vardas, P., Townsend, N., Torbica, A., Katus, H., De Smedt, D., Gale, C. P., Maggioni, A. P., Petersen, S. E., Huculeci, R., Kazakiewicz, D., de Benito Rubio, V., Ignatiuk, B., Raisi-Estabragh, Z., Pawlak, A., Karagiannidis, E., Treskes, R., Gaita, D., Beltrame, J. F., … Sebastiao, D. (2022). European Society of Cardiology: Cardiovascular disease statistics 2021. *European Heart Journal*, *43*(8), 716–799. https://doi.org/10.1093/eurheartj/ehab892

Townsend, D. W. (2008). Positron Emission Tomography/Computed Tomography. *Seminars in Nuclear Medicine*, *38*(3), 152–166. https://doi.org/10.1053/j.semnuclmed.2008.01.003

Townsend, N., Kazakiewicz, D., Lucy Wright, F., Timmis, A., Huculeci, R., Torbica, A., Gale, C. P., Achenbach, S., Weidinger, F., & Vardas, P. (2022). Epidemiology of

cardiovascular disease in Europe. *Nature Reviews Cardiology*, *19*(2), 133–143. https://doi.org/10.1038/s41569-021-00607-3

Warmink, K., Siebelt, M., Low, P. S., Riemers, F. M., Wang, B., Plomp, S. G. M., Tryfonidou, M. A., van Weeren, P. R., Weinans, H., & Korthagen, N. M. (2022). Folate Receptor Expression by Human Monocyte–Derived Macrophage Subtypes and Effects of Corticosteroids. *CARTILAGE*, *13*(1), 194760352210814. https://doi.org/10.1177/19476035221081469

White, H. D., & Chew, D. P. (2008). *Acute myocardial infarction*. *372*, 15.

Withers, P. J., Bouman, C., Carmignato, S., Cnudde, V., Grimaldi, D., Hagen, C. K., Maire, E., Manley, M., Du Plessis, A., & Stock, S. R. (2021). X-ray computed tomography. *Nature Reviews Methods Primers*, *1*(1), 18. https://doi.org/10.1038/s43586-021-00015-4

World Health Organization. (2022). *World health statistics 2022: Monitoring health for the SDGs, sustainable development goals*. World Health Organization. https://apps.who.int/iris/handle/10665/356584

Yusuf, S., Pearson, M., Sterry, H., Parish, S., Ramsdale, D., Rossi, P., & Sleight, P. (1984). The entry ECG in the early diagnosis and prognostic stratification of patients with suspected acute myocardial infarction. *European Heart Journal*, *5*(9), 690–696. https://doi.org/10.1093/oxfordjournals.eurheartj.a061728

Zeissler, C. J., Lindstrom, R. M., & McKinley, J. P. (n.d.). *Radioactive particle analysis by digital autoradiography*.

Zhang, Z., Tang, J., Cui, X., Qin, B., Zhang, J., Zhang, L., Zhang, H., Liu, G., Wang, W., & Zhang, J. (2021). New Insights and Novel Therapeutic Potentials for Macrophages in Myocardial Infarction. *Inflammation*, *44*(5), 1696–1712. https://doi.org/10.1007/s10753-021-01467-2